MSc Environomical Pathways for Sustainable Energy Systems - SELECT

MSc Thesis

Numerical resolution of heat transfer phenomena in high temperature solar thermal power applications

Author: Victor Montes de Oca Córdova

Supervisors:

Principal supervisor: Assensi Oliva Llena

Session: August 2013

Escola Tècnica Superior d'Enginyeria Industrial de Barcelona

UNIVERSITAT POLITÈCNICA DE CATALUNYA

MSc SELECT is a cooperation between

KTH-Royal Institute of Technology, Sweden | Aalto University, Finland | Universitat Politècnica de Catalunya, Spain | Eindhoven University of Technology, Netherlands | Politecnico di Torino, Italy | AGH University of Science and Technology, Poland | Instituto Superior Técnico, Portugal

Abstract

The main topic of this thesis work is the resolution of fluid mechanics phenomena via numerical methods. It is intended to use the knowledge acquired in the resolution of transfer phenomena for concrete applications in the solar energy sector, specifically, Concentrated Solar Power installations. The first part of the work lists motivations behind the use of renewables and the different alternatives and configurations in solar thermal energy generation. In the numerical resolution section, the governing equations describing flow motion are listed and described: continuity, momentum and energy. These equations are thoroughly analyzed and solved via a set of exercises comprising: heat conduction, convection-diffusion given a flow field, lid driven cavity problem and finally a natural convection exercise. Each section presents the discretization method, integration technique, numerical parameters, grid geometry and benchmark comparison. Additionally, the procedure to solving problems with unstructured grids is presented via a new discretization formulation. Finally in the Turbulence insights section, some topics regarding this chaotic phenomenon are described.

Table of Contents

Glossary

A	surface	Re	Rayleigh number
α	Thermal diffusivity	Ra	Rayleigh number
f	Face indicator	Pr	Prandtl number
$\dot{m}$	Mass flow	Nu	Nusselt number
Γ	Diffusion coefficient	$\vec{g}$	Gravity vector
ρ	Density	u	Internal energy
c_p	Specific heat	$\vec{u}$	Velocity vector
k	Thermal conductivity	β	Volumetric thermal expansion coefficient
h	Enthalpy	κ	Fourier coefficient
μ	Viscosity	Ω	Volume
ν	Kinematic viscosity	d_{ij}	Distance from i to j
P_e	Péclet number		
P	Pressure		

Numerical resolution of heat transfer phenomena in high temperature solar thermal power applications

Victor Montes de Oca Córdova

August, 2013

1. Introduction

The energy use

Throughout history, societies have relied on energy to improve their living conditions. The ability to produce and control fire represented a huge step towards evolution for the primitive man. Fire allowed early humans to cook food, stay warm in cold weathers and improve agricultural productivity (1). As the centuries passed, it was evident that at every stage in human history new fuels and ways to produce energy were also invented. Examples of this include wood, charcoal and peat. In the second half of the 18thcentury, James Watt created the first steam engine. This landmark event would represent the beginning of the Industrial Revolution. It was during this period that the need for fuels, specifically coal, increased dramatically (2). The modern technologies brought an expansion in the use of fossil fuels in the 19th and 20th centuries (1). In most modern countries, the well-being of the population depends greatly on a secure and adequate supply of energy. Energy is present and drives all of our needs: transportation, industry, education, and healthcare, among others.

In order to have an idea of the modern energy statistics, two quantities are very useful: The Total Primary Energy Supply (TPES) and the Total Final Consumption. According to the International Energy Agency (IEA), the world TPES was 12717 million tons of oil equivalent (MTOE) (1TWh = 0.086 MTOE) (3). This quantity includes all the energy production from fuels such as oil, natural gas, coal, hydropower, etc. The total final consumption accounts for the energy losses when transforming the produced energy into useful power. In 2010 the world's total final consumption was 8677 MTOE. Figure 1.1 shows the yearly trend of energy consumption by fuel.

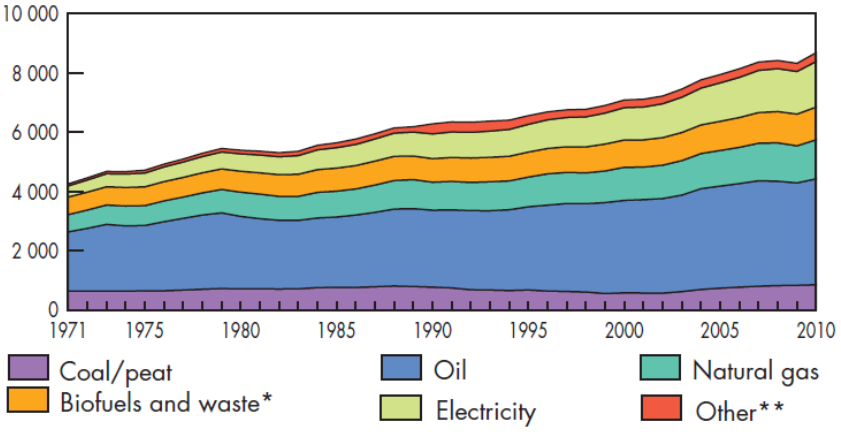

Figure 1.1. Yearly energy consumption by fuel in MTOE (3).

With a world population continually growing, the demand for energy is also increasing. In 2010, the average energy supply per capita was 1.86 TOE (3). On the other hand the average electricity consumption per capita was 2892 kWh. Evidently, these numbers change drastically according to the development status of each country.

1.1.1. Fossil fuels

Fossil fuels are formed due to the decomposition of organic matter. For millions of years, earth accumulated underground energetic reserves with high percentages of carbon. The main fossil fuels used nowadays are: coal, natural gas and oil (4). These three fuels combined represent almost 81% of the TPES (3). Due to the high energetic content, fossil fuels have been successfully used throughout history. Oil and its byproducts in particular (gasoline, Diesel, etc.), have been successfully used in the 20th century for they are safe, easy to carry and reliable source of energy (5).

After World War II, countries relied on a continuous and cheap supply of oil which allowed a constant industrial expansion (6). In 1973, political disagreements derived in a major oil crisis. Some of the biggest oil producing countries imposed an embargo on the United States which in turn, brought escalate in oil prices (6). This is arguably, the first time in history where the society started paying attention to new energy options. However the shift from oil towards different energetic options is due to two main reasons: sustainability and availability.

Environmental Concerns

Due to their composition, fossil fuels release different emissions when combusted. One of these pollutants is carbon dioxide (CO_2) (7). CO_2 is a compound that is produced by the earth and living organisms. Carbon dioxide is used along with sunlight by plants during photosynthesis. As a carbon compound, CO_2 is also part of the carbon cycle. This process occurs naturally and it refers to the exchange of carbon between the different constituent parts of earth: biosphere, atmosphere, hydrosphere, etc (8). When fossil fuels are burned, they create a new flux of carbon to the cycle. Since this new flux is not compensated during absorption, the CO_2 concentrations are slowly increased in the atmosphere (8). The excessive concentration of CO_2 and other pollutants damage the ozone layer whose function is to prevent harmful ultraviolet light from reaching living organisms from earth. Figure1. 2 shows the evolution of CO_2 concentrations in the atmosphere over the years.

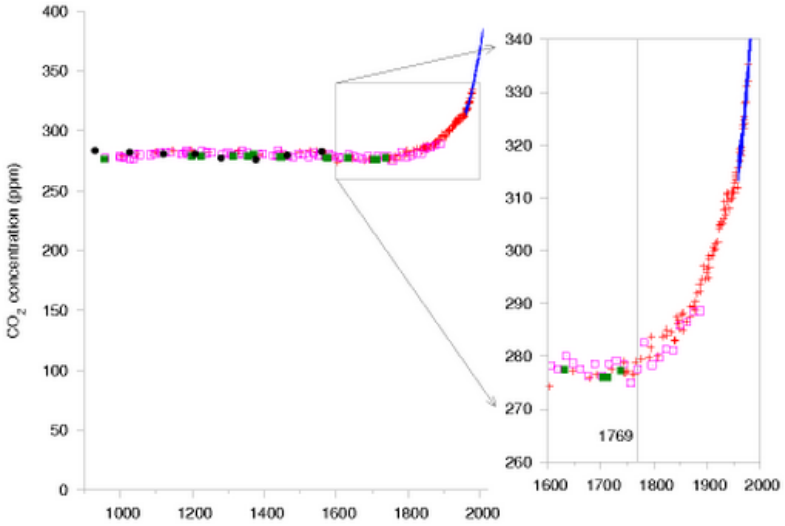

Figure 1.2. Carbon dioxide concentrations for the last 1100 years (9).

Another impact is the increase on earth temperature caused by the global warming due to the greenhouse effect. Solar radiation strikes earth in a continuous way. Some of this radiation is reflected by the earth's surface to outer space. However some of this radiation is reflected back to the surface of the earth by the greenhouse gases, mainly the ozone layer. The greenhouse effect is a natural phenomenon that is needed in order to preserve a stable temperature that allows life on earth. The problem arises, when the greenhouse gases are increased due to anthropogenic emissions (10). When this occurs the greenhouse effect is scaled up, bringing undesired heat fluxes and thus increasing the temperature of the earth surface. The consequences of climate change are manifold. The extremes in weather conditions harm the food supply, geographical settlements and ecosystems in general (11).

Availability concerns

The current use of fossil fuels is also constrained by the availability of resources. For years the production of petroleum and derivatives increased as a function of demand and the constant discovery of wells. In 1956 M. King Hubbert proposed the theory of peak oil. This theory predicts the point in time where the extraction rate of petroleum is reached. After this point the extraction rate will decline permanently until reaching to the total depletion of the finite natural resource (12). Figure 3 shows the oil production in million barrels as a function of time. It is possible to notice the constant negative slope in production over the years. The curve fit approximation predicts total resource depletion in approximately 50 years.

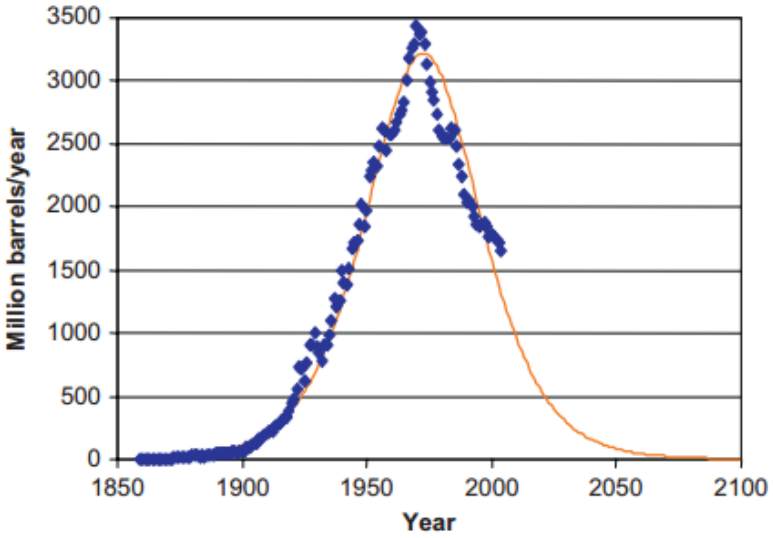

Figure 1.3. Petroleum production over the years and future estimation (12)

Solar energy

The sun is the driving force of life on earth. The entire present ecosystem in our planet is a result of the everlasting effects of the sun. Ultimately, every available energy resource is a product of the solar irradiation. For instance, wind moves as a result of pressure changes that are product of temperature gradients due to solar influence (13). Biomass consists of plants that use sunlight during photosynthesis. On the other hand fossil fuels were once living organisms that were nourished by the sun in a similar way (4). From early times, men have tried to find a way to make the most out of its interaction with solar energy. Agriculture and construction are just broad examples of how primitive man realized on the importance of the sun.

As a radiant body, the sun emits energy in the way of light and heat. Every day the earth is struck with radiation in different parts of the solar spectrum. This solar spectrum resembles the one of a black body with a temperature of 5777 Kelvin (14). Figure 1.4 shows the spectral distribution of the sun for different wavelengths and the comparison of a blackbody at the specified temperature.

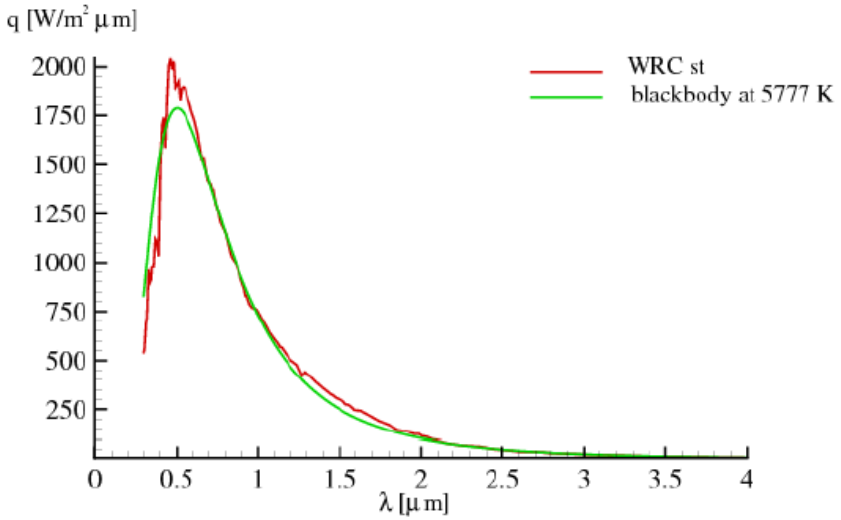

Figure 1.4. Solar spectrum at the top of the atmosphere and black body radiation at 5777 K. (14)

It is important to mention that the sun emits mostly in the ultraviolet and infrared spectrums but mainly in the visible range. Just outside the earth's atmosphere, the solar irradiation has a value of 1366 W/m^2.This value is known as the solar constant. Due to different atmospheric phenomena like scattering, absorption or diffraction this value is reduced depending to the meteorological conditions within the atmosphere (14). In order to calculate the approximate solar radiation on the surface on earth, empirical models have been created taking as inputs: place, date and time. As a result of the difference in latitudes, not all regions of the world have the same level of irradiation. The regions close to the Equator usually show a greater level of irradiation per meter square. A map with the average solar irradiation in Europe is illustrated in Figure 1.5.

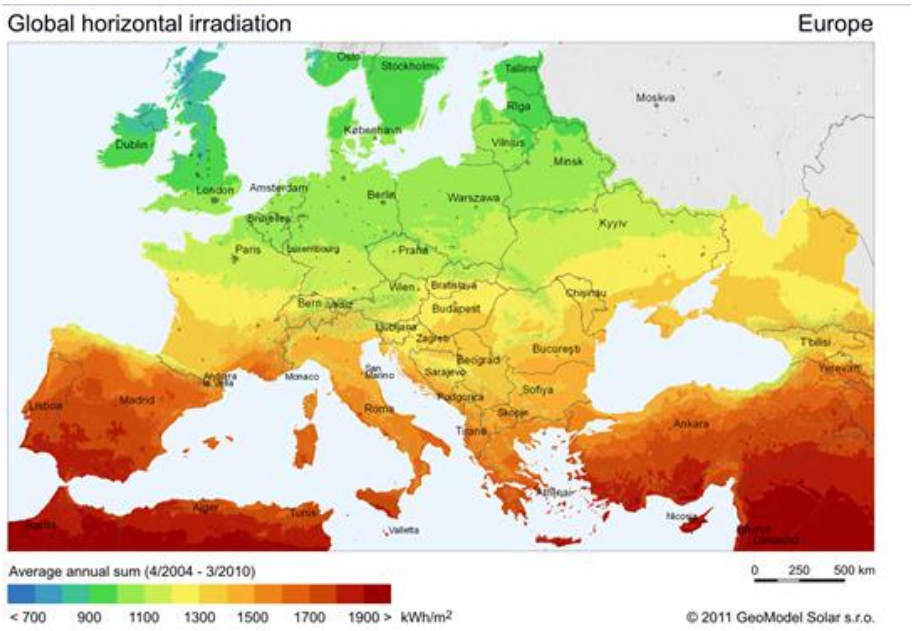

Figure 1.5. Average annual irradiation in Europe (15).

Concentrated Solar Power (CSP)

Concentrated solar power systems use the sun irradiation as a source of thermal energy and convert it into useful power. As the name suggests, (16). Though the technology is still in a developing state, great advances in installed capacity make CSP a promising and clean alternative. There are different technologies to concentrate sunlight to produce heat like: parabolic trough, solar power tower, Fresnel reflector or Dish Stirling. The first two technologies are the most broadly used and will be briefly described below:

1.1.2. Parabolic trough

This technology features large fields of mirrors that concentrate sunlight in a specific point. The mirrors have parabolic shape and the irradiation is reflected into a tube (receiver) that is placed in the focal point of the parabola. Inside the receiver, a circulating fluid removes the heat and transfers it to a power block where in turn is transformed into electricity (17). A parabolic through system can be improved with thermal storage system. Good efficiencies depend on the concentration ratio of the mirrors as well as their reflectivity. The heat transfer fluid can be water for direct steam generation plants, whereas oil or molten salts for indirect generation plants. Figure 1.6 shows the usual configuration of the mirror and receiver.

Figure 1.6. Parabolic trough concentrated solar power

1.1.3. Solar Tower

The other mainstream application of CSP is the concept of Solar Power Tower. Unlike the parabolic trough, the solar tower system concentrates the sunlight into a receiver mounted on top of a tower. The irradiation is directed to the receiver through a field of reflecting mirrors (heliostats) that are capable of tracking the Sun's path in the horizon. Each heliostat is composed of several individual flat mirrors that are placed strategically on the field to reflect as much sunlight as possible (18).

In a typical solar tower installation, a heat transfer fluid is transferred from a 'cold tank' container to the receiver. In the receiver, the incident radiation makes the fluid to absorb the heat and thus increase its temperature. Then, the fluid can be directed to a heat exchanger to transfer the thermal energy to water in order to produce steam that is necessary to run a turbine within a power cycle. The hot fluid can also be directed to a 'hot tank' where the heat is stored and kept for future use when there is no available irradiation.

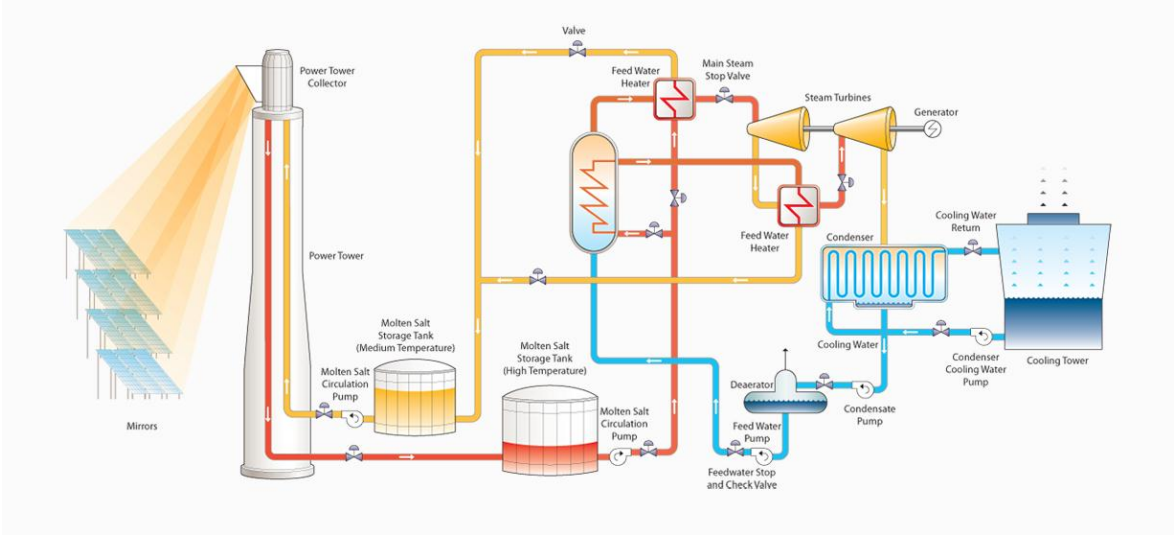

Figure 1.7. Concentrated solar tower plant configuration (19)

Thermal storage can significantly increase the capacity factor of the power plant. Figure 1.7 shows a typical configuration of the solar tower power plant.

1.1.3.1. Solar tower receivers

There are two main types of solar tower receivers: external and cavity. External receivers feature heat transfer tubes surrounding the perimeter of the structure. Cylindrical receivers are common examples of external configurations. In order to decrease the convection losses, the cavity receiver is placed in the back wall of an enclosed space (20). In Figure 1.8, an example of a cavity receiver is provided.

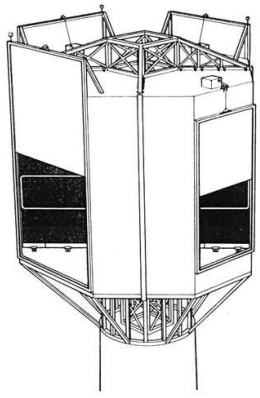

Figure 1.8. Solar tower cavity receivers (20).

Master thesis overview

Solar thermal alternatives have proven to be a realistic and efficient way to harvest sunlight. However CSP technologies are mainly within experimental or developing phases and the areas of opportunity for analysis and design are manifold. Heat losses affect negatively the efficiency of any thermal device. Considering the size of most CSP applications, solar tower receivers are also affected by the three heat transfer mechanisms: conduction, convection and radiation. In order to estimate these losses is necessary to know the transport mechanisms found in fluid flow. This master thesis can be considered as a preliminary study of the numerical resolution of heat transfer and fluid flow phenomena. The knowledge acquired with this work will be subsequently used in any related CSP project dealing mainly with heat losses in solar tower cavity receivers.

To investigate heat losses an establishment of the differential equations that describe the conservation principles is needed. Once the main partial differential equations have been set it is possible to proceed to their resolution. In order to do so, the treatment will be performed in the following way. First, the energy equation will be addressed with special attention to the conduction term. Afterwards, the convective part of the equation will be introduced by setting a given velocity field. In the next section, the momentum equation will be addressed by a lid driven cavity problem. Finally, a combination of momentum and energy equation will be used when solving natural convection in a differentially heated cavity. The last chapters deal with the resolution of unstructured grids and the introduction to turbulent flows. In all the presented problems, different integration and discretization techniques will be introduced and discussed.

2. Governing differential equations

The behavior of the physical phenomena found in heat transfer and fluid motion begins with the establishment of the system characterization in mathematical form. This process is done mainly with the establishment of partial differential equations. In this chapter the main conservation laws are presented and the equations derived from them are listed and explained.

The transport equation

When a system is being analyzed, either macroscopically, microscopically or at a molecular level several relations between their properties must be assessed in order to describe the system. Different laws and theories have proven themselves fundamental in order to study the dynamics of flows. Conservation laws, state that certain properties within a system remain unchanged in the course of time (21). In this work, the analysis will be limited to the mass, momentum and energy conservation laws. The mass conservation law states that the amount of mass that enters and leaves a closed system has to remain constant over time (22). In other words, it implies that matter cannot be created nor destroyed. The second principle is the linear momentum conservation. Derived from Newton's laws of motion, it implies that the total momentum is conserved in closed systems. Finally the same aforementioned principles are applied to the system total energy.

The properties of a system can also be described mathematically via a partial differential equation. If ρ represents density and ϕ is considered as a dependent variable, the general transport differential equation reads as following:

$$\frac{\partial(\rho\phi)}{\partial t} + \nabla \cdot (\rho\vec{u}\phi) = \nabla \cdot (\Gamma\nabla\phi) + S \qquad \text{(Eq. 2.1)}$$

In the previous equation, $\vec{u}$ represents a velocity vector, S a source term and Γ is the diffusion coefficient. There are four basic elements in the convection-diffusion equation: transient term, convection term, diffusion term and source term. The aforementioned elements will receive special analysis in the coming sections.

In order to proceed with the problem resolution, it is necessary to define which set of equations are needed to solve heat transfer and fluid flow phenomena. For this work, the momentum and energy equations will be used extensively. However it is important to notice that the general convection-diffusion equation can provide more information such as conservation of chemical species.

The energy equation

This partial differential equation accounts for the transport of energy in a homogenous fluid or a solid. It is especially important because it allows solving problems dealing with non-isothermal systems. Indeed, the most useful form of the energy equations is the one when it is possible to obtain the temperature. In this moment, the details of the derivation will be skipped to focus on the solving of the equations. Considering h as the system enthalpy, S the volumetric rate of heat generation and neglecting the viscous dissipation, the general transient energy equation is shown below.

$$\frac{\partial(\rho h)}{\partial t} + \nabla \cdot (\rho \vec{u} h) = \nabla \cdot (\mathrm{k} \nabla T) + S \qquad \text{(Eq. 2.2)}$$

The third element in the energy equation is a well-known term that describes heat conduction. It is called Fourier's law and it describes the transport of heat in an isotropic media. The symbol k stands for the thermal conductivity of a particular material (23).

$$\vec{q} = -k \nabla T \qquad \text{(Eq.2.3)}$$

The equation of motion

In order to describe the conservation of momentum in fluids a partially differential equation is also used. This set of equations is named after two important fluid scientists and are also known as the Navier-Stokes equations. The equation of motion below makes several important assumptions: the equation is given for an incompressible fluid. This concept will be further explained in the continuity equation section. Furthermore in the diffusive part of the equation it is possible to recognize the Newton's law of viscosity. This law establishes that the fluid shear force per unit area is proportional to the product of viscosity and the negative of the velocity gradient (Eq.2. 5). The equation also features the gradient of the pressure and the gravity acting as an external force. It is important to mention that the solution of the Navier-Stokes equations is given in the form of velocity fields.

$$\frac{\partial(\rho \vec{u})}{\partial t} + \nabla \cdot (\rho \vec{u} \vec{u}) = \mu \Delta \vec{u} - \nabla p + \rho \vec{g} \qquad \text{(Eq.2.4)}$$

$$\tau = -\mu(\nabla \vec{u} + (\nabla \vec{u})^{*}) \qquad \text{(Eq.2.5)}$$

The continuity equation

The continuity equation is a consequence of the mass conservation law. As previously mentioned it implies that the amount of mass in a closed system has to remain constant over

time. The previous energy and momentum equations have to satisfy this continuity constraint.

$$\frac{\partial \rho}{\partial t} + \nabla \cdot (\rho \vec{u}) = 0 \qquad \text{(Eq.2.6)}$$

A special form of the continuity equation happens when the density is considered as constant. In that case the fluid is called incompressible and the equation is reduced to the following form:

$$\nabla \cdot \vec{u} = 0 \qquad \text{(Eq.2.7)}$$

3. Heat conduction

The transfer of thermal energy in a media is caused by the interaction of its molecules due to a temperature gradient (23). Since it is presents in solids, liquids and gases, heat transfer via conduction is a fundamental process in most engineering applications. This section describes the mathematical formulation of heat conduction. Furthermore a problem is proposed to evaluate the numerical resolution of this kind of heat transfer.

Governing equations

The analysis begins introducing the energy equation. In this case, the kinetic and potential energy of the system are left out and we only focus on the internal energy as seen in equation 3.1.

$$\frac{\partial(\rho u)}{\partial t} + \nabla \cdot (\rho \vec{u} u) = -(\nabla \cdot \vec{q}) + S \qquad \text{(Eq. 3.1)}$$

Some early assumptions for this case are presented. First, the Fourier's law will be introduced: it states that the heat transfer rate is equal to a thermal conductivity multiplied times the gradient of the temperature. Then, introducing the definition of enthalpy and considering a static environment the energy equation now reads:

$$\frac{\partial(\rho h)}{\partial t} + \nabla \cdot (\rho \vec{u} h) = k\Delta \mathrm{T} + S \qquad \text{(Eq. 3.2)}$$

$$\rho c_p \frac{\partial T}{\partial t} = k\Delta T + S \qquad \text{(Eq. 3.3)}$$

The incorporation of the transient term depends if the problem deals with steady or unsteady term. In a similar way, the constant "S" is included only if the problem specifies a volumetric rate of heat generation. To further illustrate the heat conduction phenomena and introduce concepts like discretization, boundary conditions and integration the following problem is proposed:

Two-dimensional transient conduction problem

A very long rod is composed of four different materials (M1 to M4). The geometry specifications and properties of the materials are given in the Tables 3.1 and 3.2 respectively. Each of the four sides of the rod interacts with the surroundings in a different way as specified in Table 3.3.

Table 3.1. Coordinates of conduction problem

	x[m]	y[m]
p_1	0.50	0.40
p_2	0.50	0.70
p_3	1.10	0.80

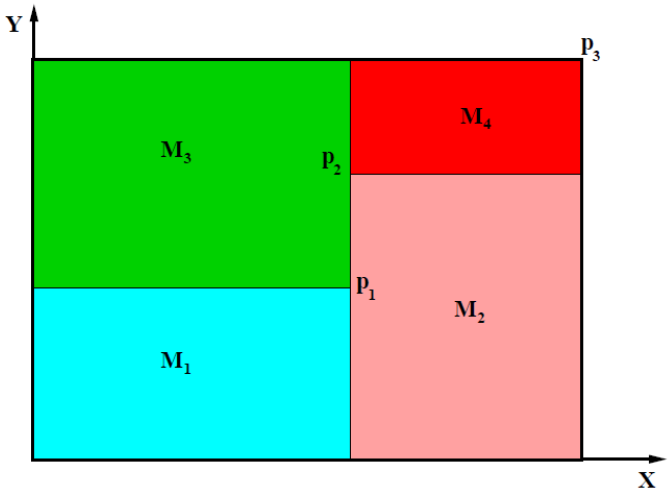

Figure 3.1. Geometry of heat conduction problem

Table 3.2. Physical properties of materials M1 to M4

	ρ (kg/m^3)	c_p (J/kg K)	k (W/m K)
M1	1500	750	170
M2	1600	770	140
M3	1900	810	200

M4	2500	930	140

Table 3.3. Boundary conditions of heat conduction problem

Cavity Wall	Boundary condition
Bottom	Isotherm at T=23.00°C
Top	Uniform Q flow = 60.00W/m length
Left	In contact with a fluid at T_g = 33.00°C and heat transfer coefficient 9.00 W/m^2 K
Right	Uniform temperature T=8.00+0.005t °C (time in seconds)

The aim of this exercise is to analyze the transient behavior of the rod. In order to check that the system is being solved in a correct way, the temperature values of two points at different locations are recorded each second. The location of point 1 is (0.65, 0.56) and point 2 (0.74, 0.72). Furthermore an instantaneous isotherms plot is provided; it was taken halfway through the simulation in order to check if the results are correct.

3.1.1. Problem resolution

Since the heat capacity, density and thermal conductivity of each material is regarded as constant and there is no source term, the energy equation to be solved is shown below:

$$\rho c_p \frac{\partial T}{\partial t} = \mathrm{k}\Delta\mathrm{T} \qquad \text{(Eq.3.4)}$$

Equation 3.4 is written in a vector form, given that the present problem will be solved using Cartesian coordinates, it is possible to represent the aforementioned equation in a Cartesian-tensor form.

$$\rho c_p \frac{\partial T}{\partial t} = k \frac{\partial^2 T}{\partial x^2} + k \frac{\partial^2 T}{\partial y^2} \qquad \text{(Eq. 3.5)}$$

The following step is to choose the adequate discretization of the domain. Since the rod is rectangular, it will be divided into several smaller control volumes. This partition will constitute the mesh of the domain. At the geometric center of each rectangle a node will be placed.

This node will be the reference point where information of the temperature will be calculated and updated according to the case. Figure 3.2 shows a schematic of a control volume for the current problem. It is possible to note that each control volume has different neighbors (4 in this case since is a two dimensional problem). Each neighbor is named after its location with respect to a reference point P.

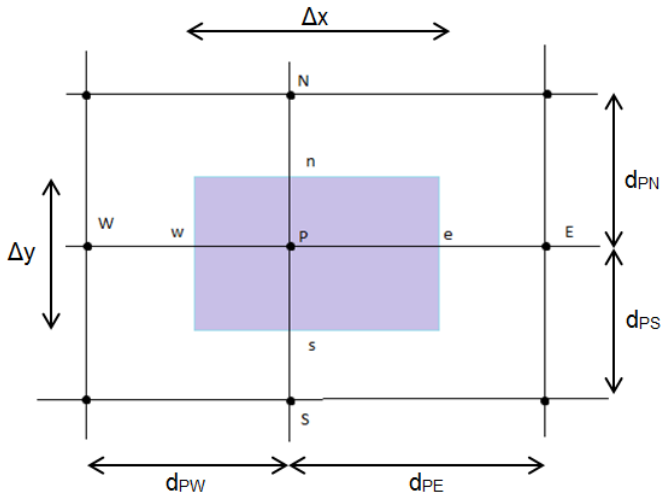

Figure 3.2. Control volume for the heat conduction problem

In figure 3.2, it is possible to notice the notation followed when defining the control volume and its neighbors. The adjacent nodes are named with a capital letter of the corresponding cardinal directions while the shared face between the controls is given a lower case.

3.1.2. Integration and discretization

The next step in the analysis is to integrate the governing equation over the whole domain of each control volume but also over time. Since the problem deals with a two-dimensional situation, it is assumed that the width of the control volume in the z direction is the unity. Furthermore the integration is performed taking as integration limits the faces of the control volume (24). The expressions for the integration of transient and diffusive term for the governing equation are shown below:

(Eq. 3.6)

$$\int_w^e \int_s^n \int_t^{t+\Delta t} \rho c_p \frac{\partial T}{\partial t} dt\, dy\, dx = \int_w^e \int_s^n \int_t^{t+\Delta t} \left[\frac{\partial}{\partial x}\left(k\frac{dT}{dx}\right) + \frac{\partial}{\partial y}\left(k\frac{dT}{dy}\right)\right] dt\, dy\, dx$$

Once the integration limits of the equation have been established, it is important to know how it is going to be solved. Let us consider the grid points in Figure 3.3: three successive grid points along the same line.

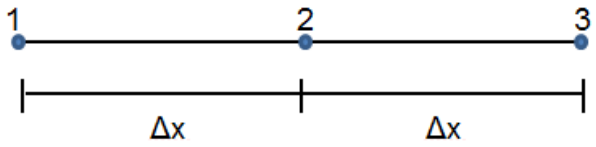

Figure 3.3. Successive points along the same line.

To approximate the derivatives present in equation 3.6 it is necessary to use a Taylor-Series formulation. If a Taylor-series expansion is performed on the variable in point 2 in Figure 3.3 the result is:

$$\phi_1 = \phi_2 - \Delta x\left(\frac{\partial \phi}{\partial x}\right)_2 + \frac{1}{2}(\Delta x)^2\left(\frac{\partial^2 \phi}{\partial x^2}\right)_2 - \cdots \quad \text{(Eq. 3.7)}$$

$$\phi_3 = \phi_2 + \Delta x\left(\frac{\partial \phi}{\partial x}\right)_2 + \frac{1}{2}(\Delta x)^2\left(\frac{\partial^2 \phi}{\partial x^2}\right)_2 + \cdots \quad \text{(Eq. 3.8)}$$

When the previous equations are added and subtracted results in the following expressions, which represent the first and second derivative with respect to x of the variable ϕ around point 2.

$$\left(\frac{\partial \phi}{\partial x}\right)_2 = \frac{\phi_3 - \phi_1}{2\Delta x} \quad \text{(Eq. 3.9)}$$

$$\left(\frac{\partial^2 \phi}{\partial x^2}\right)_2 = \frac{\phi_3 + \phi_1 - 2\phi_2}{(\Delta x)^2} \quad \text{(Eq. 3.10)}$$

Once we know how to approximate these expressions, it is possible to proceed with the integration of the governing heat transport equation. First, the integration will be done over the physical space and afterwards over time. The results of the integration for transient and diffusive term can be seen in the following equations.

$$\int_w^e \int_s^n \int_t^{t+\Delta t} \rho c_p \frac{\partial T}{\partial t} dt\, dy\, dx = \int_t^{t+\Delta t} \rho c_p \frac{\partial T}{\partial t} \Delta V \quad \text{(Eq.3.11)}$$

$$\int_t^{t+\Delta t} \left[\left(\frac{T_E - T_P}{d_{EP}} \right) \Delta y - \left(\frac{T_P - T_W}{d_{PW}} \right) \Delta y + \left(\frac{T_N - T_P}{d_{NP}} \right) \Delta x - \left(\frac{T_P - T_S}{d_{PS}} \right) \Delta x \right] dt \quad \text{(Eq. 3.12)}$$

The next step in the process is to integrate over time and choose which scheme will be used to march in time. In the forthcoming sections n+1 will refer to a new or updated value at time t+Δt, while n will make reference to the old or previous value at time t. After integration in time, and combining equations 3.11 and 3.12 the result is the following.

$$\rho c_p \frac{T_P^{n+1} - T_P^n}{\Delta t} \Delta V =$$

$$\beta \left[k_e \left(\frac{T_E - T_P}{d_{EP}} \right) \Delta y - k_w \left(\frac{T_P - T_W}{d_{PW}} \right) \Delta y + k_n \left(\frac{T_N - T_P}{d_{NP}} \right) \Delta x - k_s \left(\frac{T_P - T_S}{d_{PS}} \right) \Delta x \right]^{n+1} +$$

$$(1-\beta) \left[k_e \left(\frac{T_E - T_P}{d_{EP}} \right) \Delta y - k_w \left(\frac{T_P - T_W}{d_{PW}} \right) \Delta y + k_n \left(\frac{T_N - T_P}{d_{NP}} \right) \Delta x - k_s \left(\frac{T_P - T_S}{d_{PS}} \right) \Delta x \right]^{n} \quad \text{(Eq.3.13)}$$

The symbol β represents a weighting factor that will take its value according to the chosen scheme. In the literature review, it was found that there are three main schemes to be considered (24). The first one is called implicit, and it assumes that the new or updated value of the variable prevails through the time step. For the implicit scheme, β=1. The second scheme is called explicit and it assumes that the value of the variable over the time step is the old one. For this scheme, the value of β is equal to 0. Finally, the Crank-Nicholson scheme postulates that there is a linear variation in the value of the variable, and therefore β = 0.5. For the present exercise, an implicit scheme will be used. Setting the value of β = 1, and given that ΔV = Δx Δy, equation 3.11 now has the following form:

(Eq. 3.14)

$$\rho c_p \frac{T_P^{n+1} - T_P^n}{\Delta t} \Delta x \Delta y = k_e \left(\frac{T_E^{n+1} - T_P^{n+1}}{d_{EP}} \right) \Delta y - k_w \left(\frac{T_P^{n+1} - T_W^{n+1}}{d_{PW}} \right) \Delta y + k_n \left(\frac{T_N^{n+1} - T_P^{n+1}}{d_{NP}} \right) \Delta x - k_s \left(\frac{T_P^{n+1} - T_S^{n+1}}{d_{PS}} \right) \Delta x$$

Before proceeding with the coefficients of the discretized equations, it is worth mentioning how the thermal conductivity k_i is calculated.

When the control volume is within one same material, the thermal conductivity is taken as constant and with a value given in the initial conditions of the problem. However, when the control volume lies adjacent to a neighbor within another material a special treatment should be taken, as illustrated in Figure 3.4 and equation 3.15.

$$k_e = \left(\frac{1-f_e}{k_P} + \frac{f_e}{k_E}\right)^{-1} \qquad f_e = \frac{(\delta x)_{e+}}{(\delta x)_e} \qquad \text{(Eq. 3.15)}$$

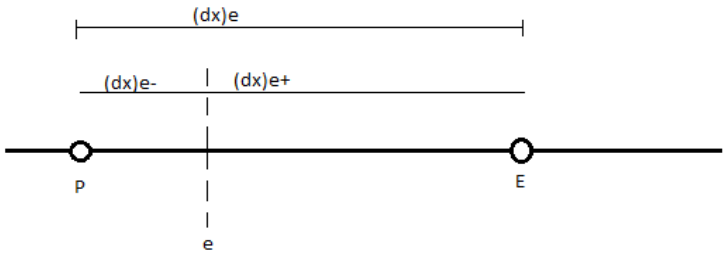

Figure 3.4. Harmonic mean schematic

The following step is to set the discretized equations to be solved. The purpose of this step is to take the equations in the form of equation 3.14 and cast them in the following way:

$$a_P {T_P}^{n+1} = a_E {T_E}^{n+1} + a_W {T_W}^{n+1} + a_N {T_N}^{n+1} + a_S {T_S}^{n+1} + b_p \qquad \text{(Eq. 3.16)}$$

Each of the discretized coefficients (a_i) is assigned the following values:

$$a_E = \frac{k_e \Delta y}{d_{EP}} \quad a_w = \frac{k_w \Delta y}{d_{PW}} \quad a_N = \frac{k_n \Delta x}{d_{PN}} \quad a_S = \frac{k_s \Delta x}{d_{PS}} \quad b_P = \frac{\rho C_P \Delta x \Delta y}{\Delta t} T_P^n$$

The coefficient a_P is composed by the addition of the neighbor discretized coefficients:

$$a_P = a_E + a_W + a_N + a_S - \frac{\rho C_P \Delta x \Delta y}{\Delta t} \qquad \text{(Eq. 3.17)}$$

3.1.3. Boundary conditions

Once the equation for the internal control volumes have been established, it is time to address those points that interact directly with the surroundings of the system. According to Patankar (24), there are three different boundary conditions in heat conduction:

- Given temperature
- Given heat flux

- Given heat flux specified via a heat transfer coefficient and the temperature of the surrounding fluid.

The first boundary condition where the value of the variable is known (in the former example, the temperature) will be known as a Dirichlet condition. The second condition, in which a heat flow is given, is known as Neumann condition. One particular case of the Neumann condition is where heat flow is equal to zero. This case deals with the ideal assumption of an adiabatic wall. The last case involves convection heat transfer between a solid and a fluid and is specified by the temperature of the fluid and the heat transfer coefficient. Now, and in accordance to the conditions in Table 3.3, it is possible to address the treatment of each wall:

- *Top Wall: Uniform Qflow*

For this wall the procedure to introduce the heat flow consisted on replace the coefficient a_N with a constant value of 0. Furthermore the, heat flow was introduced in the b_p coefficient. The heat flow value was multiplied times the length of the corresponding control volume.

- Bottom Wall: Isotherm at T=23.00°C

For this wall the Dirichlet condition was used. The south coefficient a_s was set to zero. The given temperature was introduced multiplied times the distance to the border in the b_p. Furthermore this new coefficient was added to the coefficient of the central node.

- *Left Wall: In contact with fluid at 33°C and h=9 W/mK*

In this situation the Newton approach to deal with boundary conditions was used. The west coefficient was replaced with the distance of the wall to the node times the heat transfer coefficient of the fluid. This west coefficient was added to the central coefficient. Afterwards the west coefficient was included to the b_p multiplied times the constant fluid temperature Tg.

- Right Wall: Uniform transient temperature T=8.00+0.005t

The treatment of this wall is similar to the bottom wall: both feature a Dirichlet condition. In this case the temperature is increasing with time. Each second a new wall temperature is calculated and then the coefficient of the discretized equation b_p is updated.

3.1.4. Solution to the discretized equations

Due to the large number of discretized equations, the system has to be solved iteratively. There are many different algorithms to solve systems of equations. In this section two methods will be described: the TriDiagonal-Matrix Algorithm (TDMA) and the Gaussian-elimination method. For the first method, the non-zero coefficients of the matrix align

themselves along the diagonals of the matrix. Each discretized equation is arranged in such a way that its new structure is:

$$a_i T_i = b_i T_{i+1} + c_i T_{i-1} + d_i \quad \text{(Eq. 3.18)}$$

The previous equation can also be arranged using the coefficients, P and Q.

$$T_i = P_i T_{i+1} + Q_i \quad \text{(Eq. 3.19)}$$

Alternatively, the previous equation reads:

$$T_{i-1} = P_{i-1} T_i + Q_{i-1} \quad \text{(Eq. 3.20)}$$

Combining equations 3.18 and 3.20 results in the following form of the equation:

$$a_i T_i = b_i T_{i+1} + c_i (P_{i-1} T_i + Q_{i-1}) + d_i \quad \text{(Eq. 3.21)}$$

The coefficients P_i and Q_i stand for the following expressions:

$$P_i = \frac{b_i}{a_i - c_i P_{i-1}} \quad \text{(Eq. 3.22)}$$

$$Q_i = \frac{d_i + c_i Q_{i-1}}{a_i - c_i P_{i-1}} \quad \text{(Eq. 3.23)}$$

It is important to notice that at the end of the sequence, the coefficient $b_N = 0$, it implies that the last element $T_N = Q_N$. The process is then performed backwards in order to obtain the temperature field of the whole domain. The TDMA is very powerful solving one dimensional systems, however when the problem includes more than one, the method has to be combined with other algorithms. As has been mentioned before, this problem deals with a two dimensional situation. In order to solve this kind of systems, the TDMA algorithm is combined with the Gaussian Elimination. Each row or column of the domain is solved individually using TDMA. The solver goes line by line of nodes solving the equations with the most updated values of the Temperatures. This procedure is done through all the lines of the domain until all the points are updated. The iterations continue until a convergence criterion is reached, as seen in the following equation.

$$\frac{T^{n+1} - T^n}{\Delta t} < \varepsilon \quad \text{(Eq. 3.24)}$$

The value of epsilon in the previous equation is usually very small. For this case is taken as 1×10^{-6}.

Analysis of the results

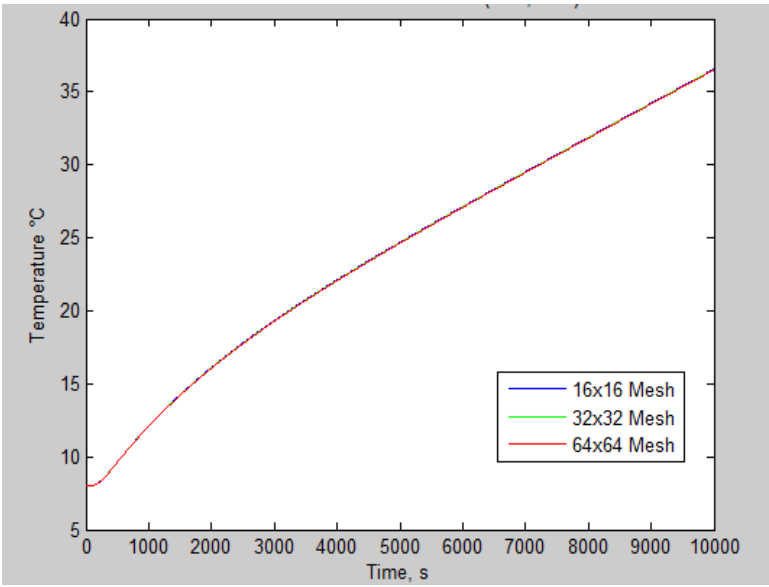

Figure 3.5. Transient evolution for point (x=0.65, y=0.56)

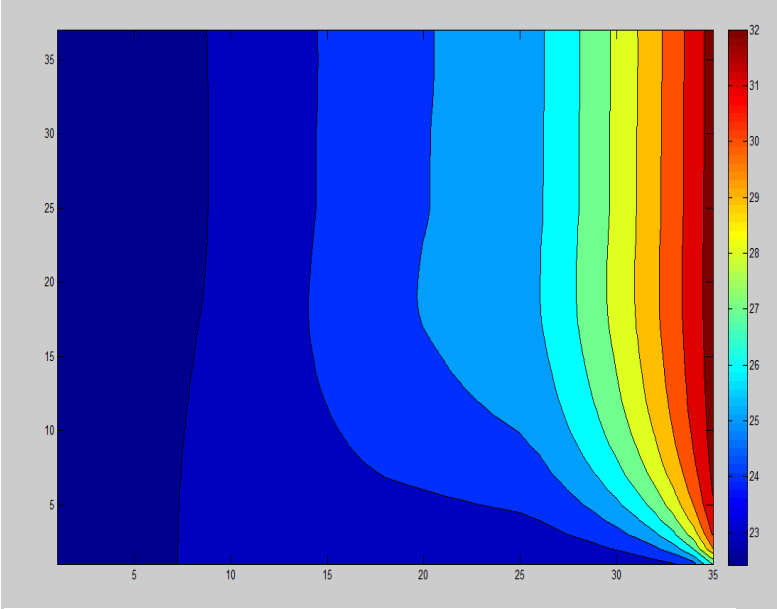

Figure 3.6. Screenshot at halfway through the simulation

Figure 3.5 shows the transient evolution of a tracking point located in the coordinates x=0.65 and y=0.56. It can be seen in the figure that the curve presents a smooth transition at the beginning of the simulation. This is noted through a change in the slope. From time=5000s

onwards, the curve presents a linear behavior. The analysis was also took into account the number of control volumes for each mesh. For this case it was found that the results are not very different from each other considering meshes consisting of 16x16, 32x32 and 64x64 control volumes. A second tracking point was located at coordenates x=0.74 and y=0.72, the results were similar to the first curve and for convenience the plot was not included in the analysis of the results. Both plots were compared with a benchmark solution and they were found to be in good agreement.

Figure 3.6 shows the isotherm plots at time = 5000 seconds. It can be appreciated how the temperature gradient is stronger on the right wall characterized with the transient Dirichlet condition. Furthermore, the top side features isothermal regions with a perpendicular profile in between regardless of the temperature on each region of the domain. Even though the regions on the right, M_2 and M_4 show the same thermal conductivity, the difference in temperature gradients is explained by the different in heat capacity, density and finally, the boundary conditions.

4. Convection and diffusion given velocity field

In the previous section the treatment of heat conduction was properly addressed and discussed. The convective part of the equation is now considered. This term accounts for the inertial forces arising from a flow in motion. First, the governing equation and theoretical background is introduced. The convective schemes will be mentioned as well as the configuration of the discretized equations. Additionally different examples will be introduced in order to clarify the numerical resolution of flows involving convection.

Background and governing equations

First, it is necessary to go back to the general transport equation:

$$\frac{\partial(\rho\phi)}{\partial t} + \nabla \cdot (\rho\vec{u}\phi) = \nabla \cdot (\Gamma\nabla\phi) + S \qquad \text{(Eq. 4.1)}$$

For the present section, the solution of the partial differential equation above will be given for the general variable ϕ (25). Furthermore, it is assumed that the velocity field is given and specified through the entire domain. The previous equation has to comply with the continuity constraint. In order to ease the explanation of the convective term, a simple assumption is made: transient and two dimensional space. For that case the governing equation takes the form:

$$\frac{\partial}{\partial t}(\rho\phi) + \frac{\partial J_x}{\partial x} + \frac{\partial J_y}{\partial y} = S \qquad \text{(Eq. 4.2)}$$

Where:

$$J_x = \rho u\phi - \Gamma\frac{\partial\phi}{\partial x} \quad and \quad J_y = \rho v\phi - \Gamma\frac{\partial\phi}{\partial y} \qquad \text{(Eq.4.3)}$$

It is possible to integrate equation 4.2 in a control volume similar to the one shown in Figure 3.2. Implying an implicit scheme, the result is shown in the equation beneath.

$$\frac{(\rho\phi_P)^{n+1} - (\rho\phi_P)^n}{\Delta t}\Delta x\Delta y + J_e - J_w + J_n - J_s = S_P^{n+1}\Delta x\Delta y \qquad \text{(Eq. 4.4)}$$

The next step is to introduce the continuity equation to achieve convergence. Recalling from equation 2.6, the continuity equation has the form:

$$\frac{\partial\rho}{\partial t} + \frac{\partial(\rho u)}{\partial x} + \frac{\partial(\rho v)}{\partial y} = 0 \qquad \text{(Eq. 4.5)}$$

Integrating over the control volume we get the following expression:

$$\frac{(\rho)^{n+1}-(\rho)^{n}}{\Delta t}\Delta x\Delta y + F_e - F_w + F_n - F_s = 0 \quad \text{(Eq. 4.6)}$$

In equation 4.6, F is the mass flow rate and equals the product of the density, the face velocity and the face surface. When equations 4.4 and 4.6 are combined the result is the following convection-diffusion equation:

$$\frac{(\rho\phi_P)^{n+1}-(\rho\phi_P)^{n}}{\Delta t}\Delta x\Delta y + (J_e - F_e\phi_P) - (J_w - F_w\phi_P) + (J_n - F_n\phi_P) - (J_s - F_s\phi_P) = S_P^{n+1}\Delta x\Delta y \quad \text{(Eq. 4.7)}$$

As can be appreciated in equation 4.7, the variable ϕ has to be evaluated at the control volume faces, which can be somehow complex to estimate. There are many available schemes to calculate the value of this variable, each with its own advantages and disadvantages. Here the general characteristics of each scheme will be mentioned.

- *Central difference scheme*

This scheme interpolates the values of the general variable ϕ from the known values of the main nodes. For instance, if the central node lays half way from both east and west nodes, the value of the variable in the faces would be:

$$\phi_e = \frac{1}{2}(\phi_E + \phi_P) \qquad and \qquad \phi_w = \frac{1}{2}(\phi_P + \phi_W) \quad \text{(Eq. 4.8)}$$

Once previous equations have been defined is possible to build discretized equations and solve for the whole domain to find the desired values. This scheme can produce unrealistic and instable solutions for highly convective regimes.

- *Upwind Scheme (UDS)*

The upwind scheme was developed as an alternative to the central difference method. In this scheme, the value of the face in the control volume takes the upstream value of the node next to it depending on the direction of the flow.

$$\phi_e = \phi_P \;\; if\; F_e > 0; \quad and \quad \phi_e = \phi_E \;\; if\; F_e < 0; \quad \text{(Eq. 4.9)}$$

Where F_e is defined as $(\rho u)_e$. After this, the discretized equations can be solved in the usual way.

- *The exact solution and Péclet number*

If the diffusion coefficient (Γ) can be taken constant there is a way to obtain an analytical solution to a flow problem. For a one dimensional situation, the exact solution is.

$$\frac{\phi-\phi_0}{\phi_L-\phi_0}=\frac{\exp\left(\frac{Pe\,x}{L}\right)-1}{\exp(Pe)-1} \quad \text{(Eq. 4.10)}$$

In the above equation Pe stands for the local Péclet number. This dimensionless number is the ratio of the strengths of convection and diffusion.

$$Pe=\frac{\rho u L}{\Gamma} \quad \text{(Eq. 4.11)}$$

When the situation is adequate, the numerical solution can be compared with the analytical solution to compare the robustness of the program.

- *The Power-Law Scheme*

The power law scheme offers a better approximation to the solution regardless of the magnitude of the Péclet number. This scheme provides a good approach of the exponential behavior without sacrificing a lot of computer memory. The discretized coefficients for the one dimensional case have the following form:

$$a_E=D_E*\max\left(0,(1-0.1|Pe_E|^5)\right)+\max(-F_E,0) \quad \text{(Eq. 4.12)}$$

It is possible to summarize the main properties of the different schemes once they are introduced in the discretized coefficients as seen on equation 4.12.

$$a_p\phi_p=a_E\phi_E+a_W\phi_W+a_N\phi_N+a_S\phi_S+b_p \quad \text{(Eq. 4.13)}$$

Where:

$$a_E=D_eA(|Pe_e|)+\max(-F_e,0) \quad \text{(Eq. 4.14)}$$

$$a_W=D_wA(|Pe_w|)+\max(F_w,0)$$

$$a_N=D_nA(|Pe_n|)+\max(-F_n,0)$$

$$a_S=D_sA(|Pe_s|)+\max(F_s,0)$$

Table 4.1 summarizes the function $A(|Pe|)$ for the aforementioned schemes:

Table 4.1. Summary of the function A(P)

Scheme	Formula for $A(\|Pe\|)$
Central difference	$1 - 0.5\|Pe\|$
Upwind	1
Exponential	$\|Pe\|/[\exp(\|Pe\| - 1)]$
Power law	$\max(0, (1 - 0.1\|Pe\|)^5)$

After the theory has been established, it is time to turn our attention into solving problems involving convection and diffusion. Several different exercises were solved covering different types of flow. For the sake of simplicity, the result and conclusions for the first 3 problems are shown and only the last exercise will be described and addressed.

One-dimenisional flow problem

The first case deals with a one-dimensional flow whose vertical walls feature a Dirichlet condition while the horizontal wall have a Neumann condition.

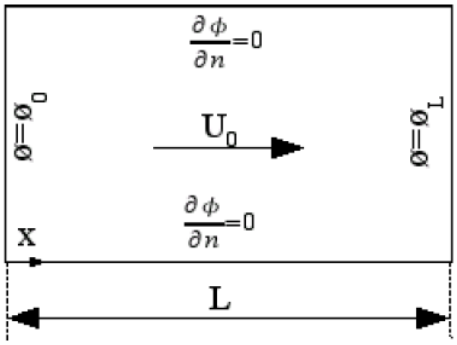

Figure 4.1. Schematic for the one-dimensional flow

Figure 4.2 shows the result of the proposed numerical solution compared with the analytical solution. The results are very similar and the difference is negligible. The developed code

featured power law scheme. As expected with this scheme, the difference between values is negligible. Several different schemes were considered and the comparison is shown in figure 4.3. In this case, upwind scheme showed the least accurate results.

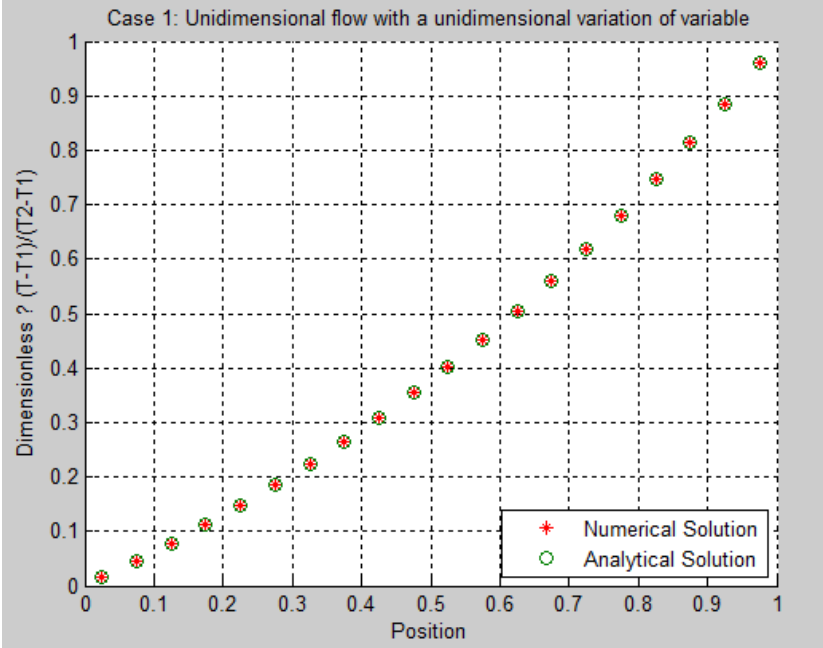

Figure 4.2. Numerical results for one-dimensional flow case

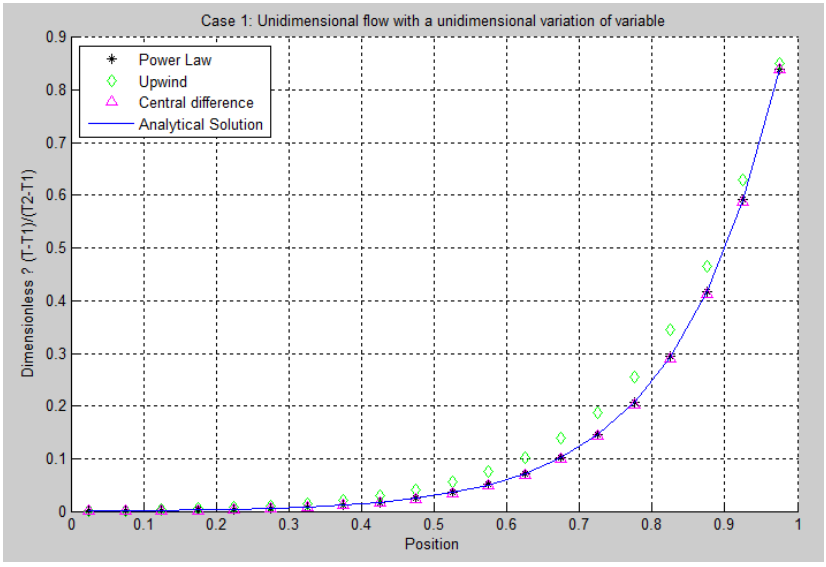

Figure 4.3. Scheme comparison for one-dimensional flow

One-dimensional perpendicular flow problem

This case is similar to the previous case regarding boundary conditions. However now, there is a perpendicular flow in the vertical direction. It was found that when the flow is perpendicular, the results of the numerical method match exactly the ones obtained with the analytical solution regardless of the scheme. Figure 4.4 shows the aforementioned fact it also possible to distinguish the linear behavior of the solution curves.

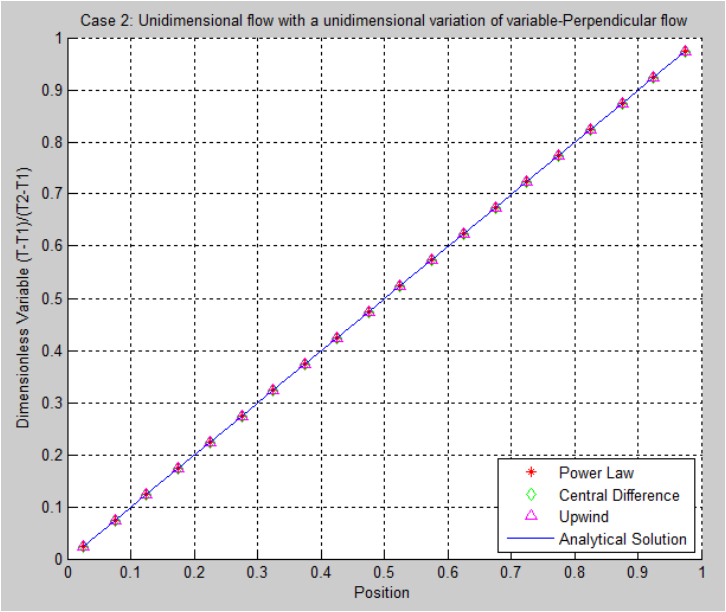

Figure 4.4. Results for one-dimensional perpendicular flow

Diagonal flow

So far the analysis has been limited to one-dimensional situations. This third case features both vertical and horizontal velocity components. For this case, the dominion has to be divided into a mesh consisting of Nx horizontal nodes and Ny vertical nodes. The diagram below shows the main components and boundary conditions for the problem. The top and left walls have the same value of the interest variable. On the other hand the right and bottom walls have the same value as well.

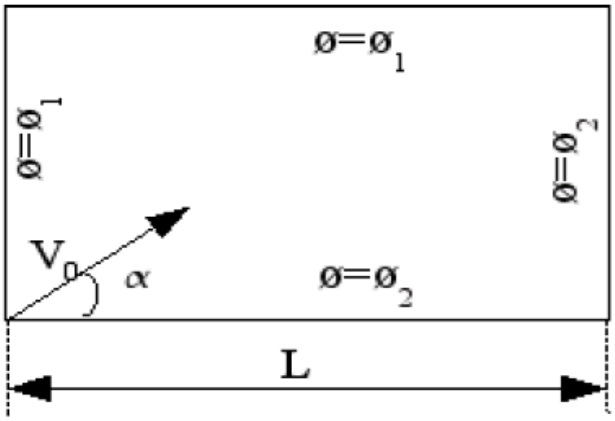

Figure 4.5. Schematic for the diagonal flow problem

For this problem a study on the influence of the mesh size will be performed. The mesh size is important in the resolution of this kind of problem because a coarse mesh might be insufficient to accurately solve all the control volumes in a domain. The solution for this problem is known at an infinite value of Péclet number.

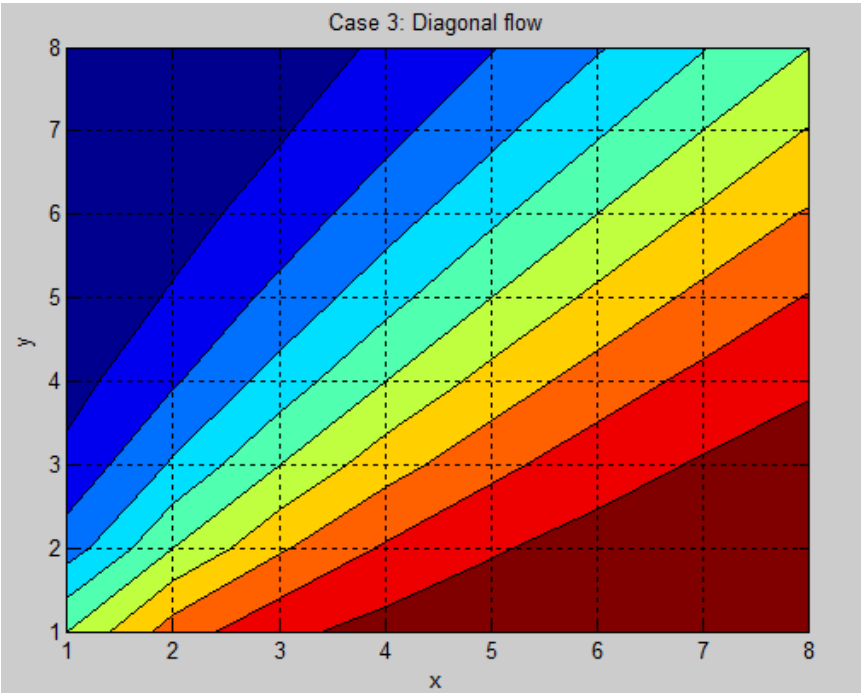

Figure 4.6. Diagonal flow at 8x8 mesh

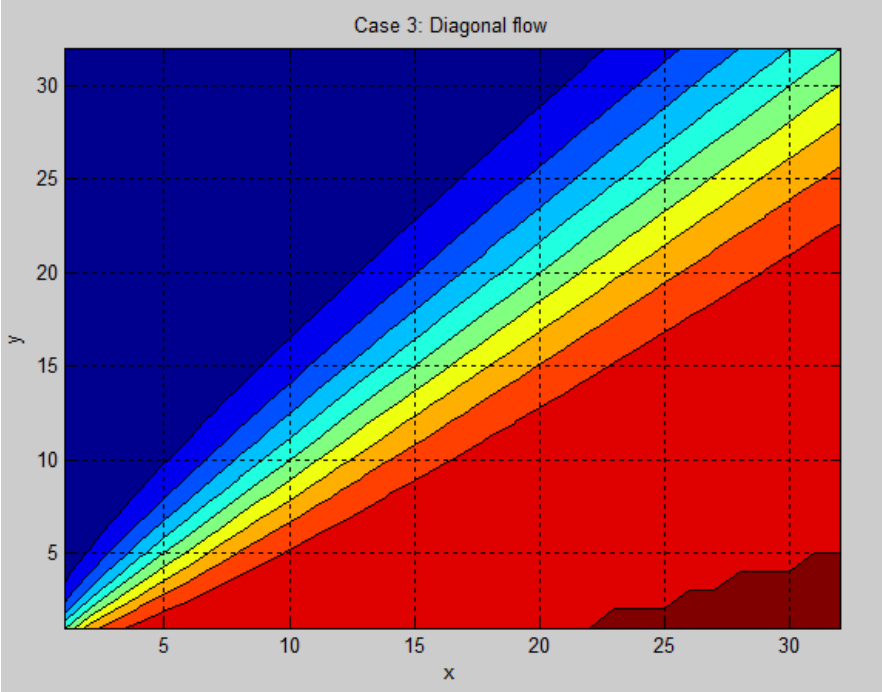

Figure 4.7. Diagonal flow, 32x32 Mesh

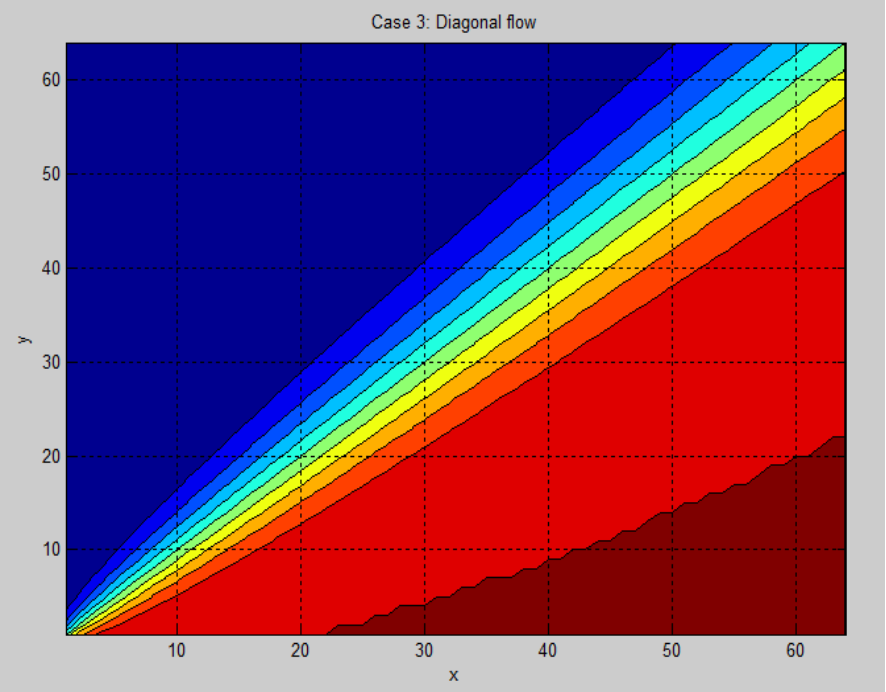

Figure 4.8. Diagonal flow, 64x64 Mesh

According to the solution given, the value of the top and left wall has to dominate the area above the diagonal, while the value of the right and bottom walls has to dominate the area below the diagonal. This can be appreciated in the three different cases, however the effect is more dramatic as the mesh is increasing in size.

Solenoidal flow

The problem to be addressed involves a rectangular cavity whose schematic and reference origin is shown in figure 21. This problem is commonly known as the Smith-Hutton problem and used to test numerical solvers.

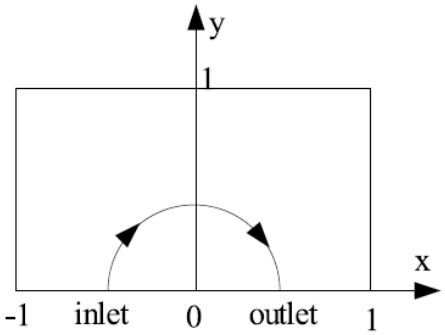

Figure 4.9. Schematic for the convection-diffusion problem

Inside the cavity there is a solenoid flow with the following position dependent velocity field:

$$u(x,y) = 2y(1-x^2) \quad \text{(Eq. 4.15)}$$

$$v(x,y) = -2x(1-y^2) \quad \text{(Eq. 4.16)}$$

The boundary conditions for the problem have to be specified in advance. For this problem table 5 summarizes the boundary conditions at the walls of the cavity with reference to the variable dependent variable ϕ.

Boundary Condition	Position	
ϕ=1-tanh(α)	x =-1	0<y<1
ϕ=1-tanh(α)	-1<x<1	y=1
ϕ=1-tanh(α)	x =1	0<y<1

$\frac{\partial \phi}{\partial y} = 0$	0<x<1	y=0
ϕ =1+tanh((2x+1)α)	-1<x<0	y=0

Table 4.2. Boundary condition for the convection-diffusion problem

In the previous table, the symbol α is a constant and has the value of 10. The objective of the exercise is to obtain the field of ϕ for the whole domain for different values of the ratio of Γ/ρ: 10, 1000 and 1000000. In all cases the mesh was composed of 128x64 nodes and feature power law scheme.

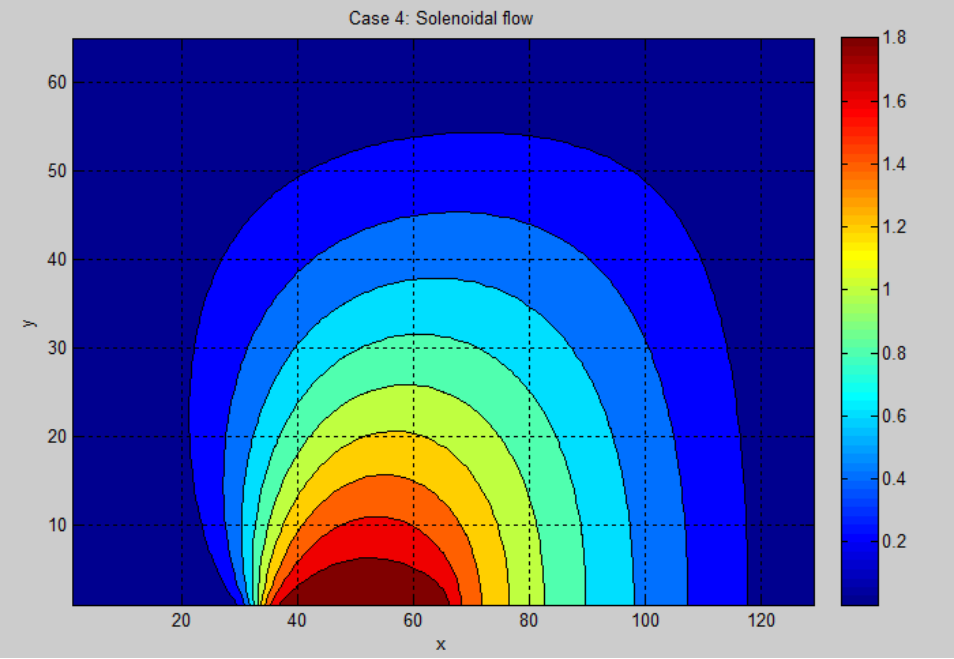

Figure 4.10. Solenoidal flow, ρ /Γ = 10

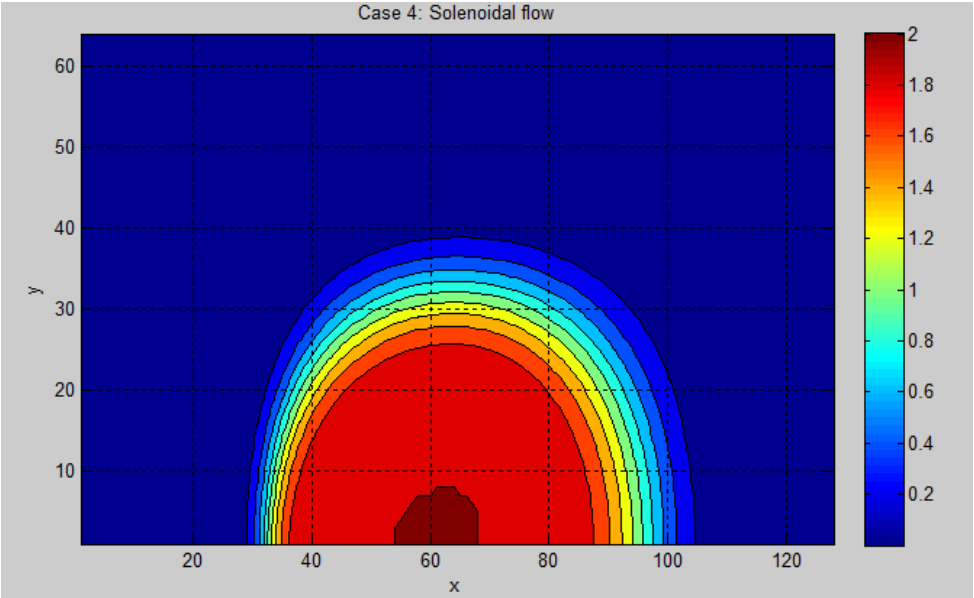

Figure 4.11. Solenoidal flow, ρ /Γ = 1000

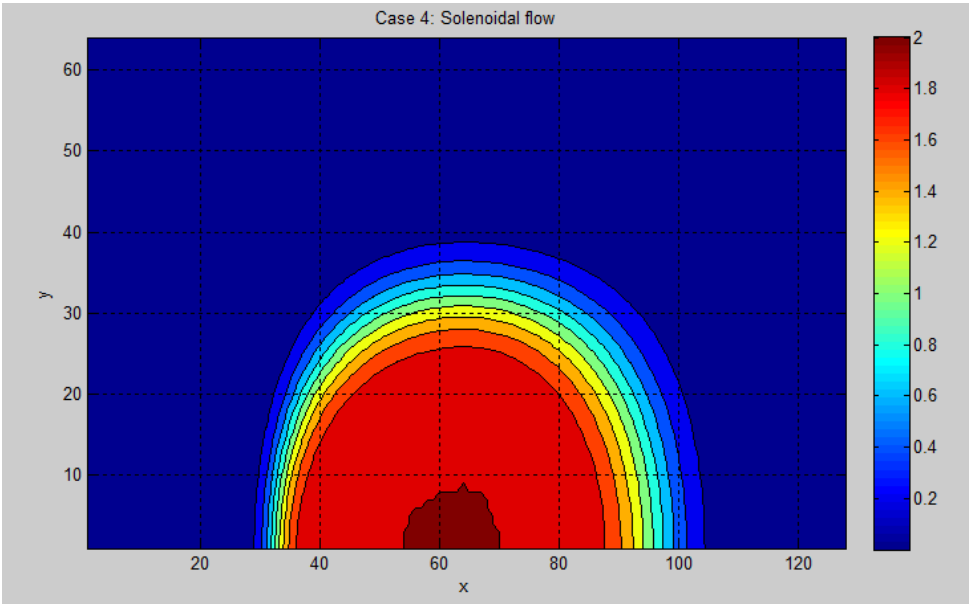

Figure 4.12. Solenoidal flow, ρ /Γ = 1,000,000

Analysis of the results

From the one-dimensional flow, it can be concluded that some schemes are more effective than others depending on how convective the flow is. In this case, since the velocity value for the presented case was low the upwind scheme results were inaccurate when compared with the analytical solution or the Power law scheme. The second exercise showed how in perpendicular flows, the numerical results were exactly the same when compared with an analytical solution. When dealing with a perpendicular flow it can be said that the distribution of the variable ϕ depends only on the boundary conditions. The diagonal flow showed how the mesh size is a relevant factor in this sort of exercises. When a finer mesh was used, the results were closer to the benchmark solution which states a diagonal division between Dirichlet values.

Finally from the Smith-Hutton problem some valuable conclusions can be drawn. First unlike the other problems, the velocity field is given via a function depending on the position within the cavity. The bottom left part of the cavity is considered as an inflow, and the bottom right can be considered an outflow. For the low Péclet number simulations (Fig. 4.10), the high concentration of ϕ area is located in the inflow of the cavity. It appears that the other medium temperature areas appear due to the effect of diffusion. On the other hand, for a high Péclet number (Fig. 4.12), the concentration of ϕ is placed uniformly in the rotational path from the inflow to the outflow of the cavity. The reader is invited to review the section 1 of the Appendix for a benchmark comparison of the values in different points in the cavity outflow.

5. The momentum or Navier-Stokes equations

In the previous sections the treatment of convection and diffusion in a general transport equation were introduced. Different numerical methods and solving strategies were used to get the general variable ϕ with or without the presence of a velocity field. For now, we turn our attention to how the velocity field is obtained through the momentum equation. In this task, the flow field of a problem has to be solved out using the momentum equation through a method called “Fractional step method”.

Governing Equations

The modeling of an incompressible flow can be done through the general conservation equation shown below:

$$\frac{\partial(\rho\phi)}{\partial t} + \nabla \cdot (\rho\vec{u}\phi) = \nabla \cdot (\Gamma\nabla\phi) + S \qquad \text{(Eq. 5.1)}$$

In order to find the required velocities, the governing equations to solve are: momentum and continuity. These equations in their dimensionless form and with primitive variables are shown below.

$$\frac{\partial\vec{u}}{\partial t} + (\vec{u}\cdot\nabla)\vec{u} = \frac{1}{Re}\Delta\vec{u} - \nabla p \qquad \text{(Eq. 5.2)}$$

$$\nabla \cdot \vec{u} = 0 \qquad \text{(Eq. 5.3)}$$

In the above equations, Re stands for the Reynolds number and is defined as the product of the density, a characteristic length and velocity divided by the dynamic viscosity.

$$Re = \frac{\rho V L}{\mu} \qquad \text{(Eq 5.4)}$$

Fractional Step Method

The essence of the fractional step method is to approximate convective and diffusive terms using a ‘predictor velocity’ (26). This velocity is calculated with no pressure gradient whatsoever. In this way the incompressibility constraint cannot be met. In order to correct so, a Poisson equation is introduced in the system to calculate the updated velocity field. The basic algorithm for the fractional step method is the following:

1. Evaluate $R(u^n)$

$$R(u^n) = -(u\cdot\nabla)u + \frac{1}{Re}\Delta u \qquad \text{(Eq. 5.5)}$$

$$R(u^n) = -\left(\frac{\partial u^2}{\partial x} + \frac{\partial uv}{\partial y}\right) + \frac{1}{Re}\left(\frac{\partial^2 u}{\partial x^2} + \frac{\partial^2 u}{\partial y^2}\right) \quad \text{(Eq. 5.6)}$$

$$R(v^n) = -\left(\frac{\partial v^2}{\partial y} + \frac{\partial uv}{\partial x}\right) + \frac{1}{Re}\left(\frac{\partial^2 v}{\partial x^2} + \frac{\partial^2 u}{\partial y^2}\right) \quad \text{(Eq. 5.7)}$$

2. Evaluate u^p

$$u^p = u^n + \Delta t\left(\frac{3}{2}R(u^n) - \frac{1}{2}R(u^{n-1})\right) \quad \text{(Eq. 5.8)}$$

3. Evaluate $\nabla \cdot u^p$ and solve the discrete Poisson equation
   $\nabla \cdot u^p = \nabla \cdot u^{n+1} + \nabla \cdot \nabla \tilde{p} \rightarrow \Delta \tilde{p} = \nabla \cdot u^p$ (Eq. 5.9)
4. Obtain the new velocity field

   $$u^{n+1} = u^p - \nabla p \quad \text{(Eq. 5.10)}$$

Lid-driven cavity problem

The lid driven cavity flow problem is commonly used to check new numerical method schemes and their accuracy. This problem can be described in the following way: an incompressible, laminar flow is enclosed in a square cavity. The top lid of the cavity moves with a constant velocity u. All the other walls can be considered static. The aim of this problem is to find the fluid velocities at different points within the cavity as a function of the fluid Reynolds number. The diagram of the situation can be appreciated in figure 25.

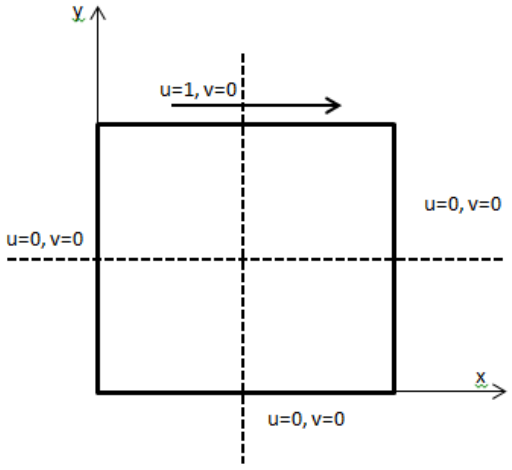

Figure 5.1. Schematic of lid driven cavity problem

Discretization equation

The next step to solve the problem is to decide the appropriate mesh and configuration for the cavity. It was chosen to work on a staggered rectangular grid. In a staggered grid, the pressure is decoupled with the velocity of the control volume. The pressure node is located in in the middle of the control volume while the velocities are located in the faces. This configuration can be appreciated in figure 5.2. The use of staggered grid prevents the apparition of unfeasible solutions arrangements such as the 'checker-board' pressure field (24).

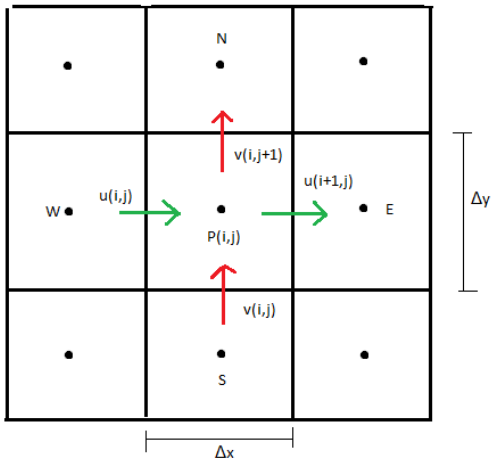

Figure 5.2. Staggered grid arrangement

The domain was divided into Nx control volumes in the horizontal direction and Ny control volumes in the vertical direction. Each node had a length of $\Delta x = Lx/Nx$ and $\Delta y = Ly/Ny$.

As can be appreciated in figure 5.2, the main velocities (u and v) are placed in the faces of the pressure control volumes. At this stage it would be convenient to highlight some initial boundary conditions, mainly impenetrability. The impenetrability boundary condition establishes that the flow velocity incident in a solid wall is 0. In a similar way the non-slip condition dictates that the velocity of the fluid will be zero relative to the boundary.

Once the geometry specifications have been settled, it is time to describe the algorithm of the fractional step method.

1. Evaluation of R(u^n)

The function R(u) includes the convective and diffusive terms of the governing equation. In order to evaluate it, it is necessary to set up a new control volume and perform integration.

This control volume will be built around the main velocities of the problem: u and v. Figure 3 illustrate these new control volumes. When the function R(u) is integrated over this control volume, the result is shown in equation 5.

$$R(u^n) = \frac{1}{\Delta x \Delta y}\left\{-[(u_e u_e - u_w u_w) * \Delta y + (v_n u_n - v_s u_s) * \Delta x] + \frac{1}{Re}\left[\frac{u_E - u_P}{\Delta x^2} - \frac{u_P - u_W}{\Delta x^2} + \frac{u_N - u_P}{\Delta y^2} - \frac{u_P - u_S}{\Delta y^2}\right]\right\} \quad \text{(Eq. 5.11)}$$

In the same fasion, the final expression for calculating R(v^n) is presented below:

$$R(v^n) = \frac{1}{\Delta x \Delta y}\left\{-[(v_n v_n - v_s v_s) * \Delta x + (v_e u_e - v_w u_w) * \Delta y] + \frac{1}{Re}\left[\frac{v_E - v_P}{\Delta x^2} - \frac{v_P - v_W}{\Delta x^2} + \frac{v_N - v_P}{\Delta y^2} - \frac{v_P - v_S}{\Delta y^2}\right]\right\} \quad \text{(Eq. 5.12)}$$

The velocities with small case letters in the above equations make reference to the velocity in the respective face of the control volume (u_n, u_s, u_e, u_w, etc.). In order to calculate the velocity in the faces, a special scheme has to be used. For simplicity the central difference scheme is used. The central difference scheme interpolates the values of the main velocity points to obtain a value for the face of the adjacent control volume. In order to simplify the indexing of the problem, the following notation was used:

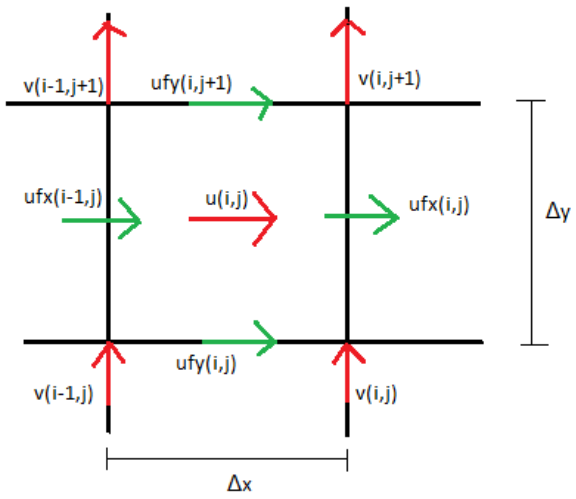

Figure 5.3 Velocity control volumen configuration

- For the u velocity: The parallel face velocities are stored in the ufx vector and the top and bottom velocities are stored in ufy. This configuration can be better appreciated in figure 3.
- For the v velocity: The parallel face velocities are stored in vfy vector and the right and left velocities are stored in vfx.

The central difference scheme for calculating the velocity in the faces is the following:

$$ufx(i,j) = \frac{1}{2}[u(i,j) + u(i+1,j)] \quad \text{(Eq. 5.13)}$$

$$vfy(i,j) = \frac{1}{2}[v(i,j) + v(i,j+1)] \quad \text{(Eq. 5.14)}$$

$$ufy(i,j) = \frac{1}{2}[u(i,j) + u(i,j-1)] \quad \text{(Eq. 5.15)}$$

$$vfx(i,j) = \frac{1}{2}[v(i,j) + v(i-1,j)] \quad \text{(Eq. 5.16)}$$

It can be appreciated in equations 5.11 and 5.12 that the convective term is multiplied times the perpendicular velocity according to the case. The same central difference scheme is used to interpolate the values of the perpendicular velocities.

$$v_n = \frac{1}{2}[v(i-1,j+1) + v(i,j+1)] \quad \text{(Eq. 5.17)}$$

$$v_s = \frac{1}{2}[v(i-1,j) + v(i,j)] \quad \text{(Eq. 5.18)}$$

$$u_e = \frac{1}{2}[u(i+1,j) + v(i+1,j-1)] \quad \text{(Eq. 5.19)}$$

$$u_w = \frac{1}{2}[u(i,j) + v(i,j-1)] \quad \text{(Eq. 5.20)}$$

2. Evaluate up

The next step in the algorithm is to find the predictor velocities u^p and ^{p}. The expression to find this velocity can be found below:

$$u^p = u^n + \Delta t\left(\frac{3}{2}R(u^n) - \frac{1}{2}R(u^{n-1})\right) \quad \text{(Eq. 5.21)}$$

$$v^p = v^n + \Delta t\left(\frac{3}{2}R(v^n) - \frac{1}{2}R(v^{n-1})\right) \quad \text{(Eq. 5.22)}$$

It is important to mention that this algorithm works under an explicit scheme. That means that Δt has to be carefully chosen in order for the whole program to converge. Convergence criteria is given by the Courant-Friedrichs-Lewey condition (CFL) (27):

$$\Delta t\left(\frac{|u_i|}{\Delta x}\right)_{max} \leq C_{conv} \quad \text{(Eq. 5.23)}$$

$$\Delta t\left(\frac{\nu}{\Delta x^2}\right)_{max} \leq C_{visc} \quad \text{(Eq. 5.24)}$$

The bounding values for C_{conv} and C_{visc} are 0.35 and 0.2 respectively. The expression $R(u^{n-1})$ makes reference the last stored value of the function R(u).

3. Evaluate $\nabla \cdot u^p$ and solve the discrete Poisson equation

The fractional step method states that in order to solve the velocity-pressure coupling it is necessary to consider the following equation:

$$u^p = u^{n+1} + \nabla \tilde{P} \qquad \text{(Eq. 5.25)}$$

Taking the divergence to both sides of the equations, and taking into account the incompressibility condition ($\nabla \cdot u^{n+1} = 0$) , the Poisson equation is now equal to:

$$\Delta \tilde{P} = \nabla \cdot u^p \qquad \text{(Eq . 5.26)}$$

Where, $\tilde{P} = \Delta t P^{n+1}$.

At this stage it is convenient to go back to the original grid: the one where the pressure nodes are located at the center of the control volume. After integration and discretization, equation 5.26 yields to the following expression:

(Eq. 5.27)

$$\frac{\tilde{P}_E - \tilde{P}_P}{d_{EP}}\Delta x - \frac{\tilde{P}_P - \tilde{P}_W}{d_{PW}}\Delta x + \frac{\tilde{P}_P - \tilde{P}_N}{d_{PN}}\Delta y - \frac{\tilde{P}_S - \tilde{P}_P}{d_{SP}}\Delta x = \frac{1}{\Delta t}\left(u_e^p \Delta y - u_w^p \Delta y + v_n^p \Delta x - v_s^p \Delta x\right)$$

It is possible now to evaluate the discretized coefficients in order to solve the equations through a direct numerical simulation. The discretized coefficients for the internal nodes of this problem are summarized below:

$$aw(i,j) = \frac{\Delta x}{d_{PW}}$$

$$ae(i,j) = \frac{\Delta x}{d_{EP}}$$

$$an(i,j) = \frac{\Delta y}{d_{PN}}$$

$$as(i,j) = \frac{\Delta y}{d_{SP}}$$

$$ap(i,j) = aw(i,j) + ae(i,j) + an(i,j) + as(i,j)$$

$$bp(i,j) = \frac{1}{\Delta t}\left(u_e^p \Delta y - u_w^p \Delta y + v_n^p \Delta x - v_s^p \Delta x\right)$$

It is time to set the adequate treatment for the boundaries. The evaluation of $\frac{\partial P}{\partial x}$ at the interface of the control volume and left and right walls equals 0. In the same way $\frac{\partial P}{\partial y}$ for top

and bottom boundaries is also 0. Therefore we can assign the coefficient of the internal nodes to the boundary ones with the following modifications:

- Top row $a_n(i,j) = 0.0$:
- Right column $a_e(i,j) = 0.0$
- Bottom row $a_s(i,j) = 0.0$
- Left column $a_w(i,j) = 0.0$

As usual the a_p coefficient for all the nodes is the sum of all the neighboring nodes after the previous modifications were made.

4. Obtain the new velocity field

Once the pressure field for the whole domain has been calculated, the new step is to obtain the updated velocity field. This is done easily with the following equations across the grid.

$$u^{n+1} = u^p - \Delta t \left(\frac{\tilde{P}_{i-1,j} - \tilde{P}_{i,j}}{\Delta x}\right) \quad \text{(Eq. 5.28)}$$

$$v^{n+1} = v^p - \Delta t \left(\frac{\tilde{P}_{i,j-1} - \tilde{P}_{i,j}}{\Delta y}\right) \quad \text{(Eq. 5.29)}$$

The velocity is then updated and the whole algorithm is repeated until convergence is achieved. As convergence criterion, the maximum difference in values between iteration for the whole domain is set to be less than 1e-8.

$$\max\left(\frac{u^{n+1} - u^n}{dt}\right) < 1e-8 \quad \text{(Eq. 5.30)}$$

After the simulation was performed, the results were analyzed and compared with a benchmark solution. In the following figures, the streamline plot for different Reynolds numbers is shown (Re=100, Re=1000, Re=5000). It is possible to observe from the plots how eddies begin to form in the corners of the cavity as a result of increasing the Reynolds number.

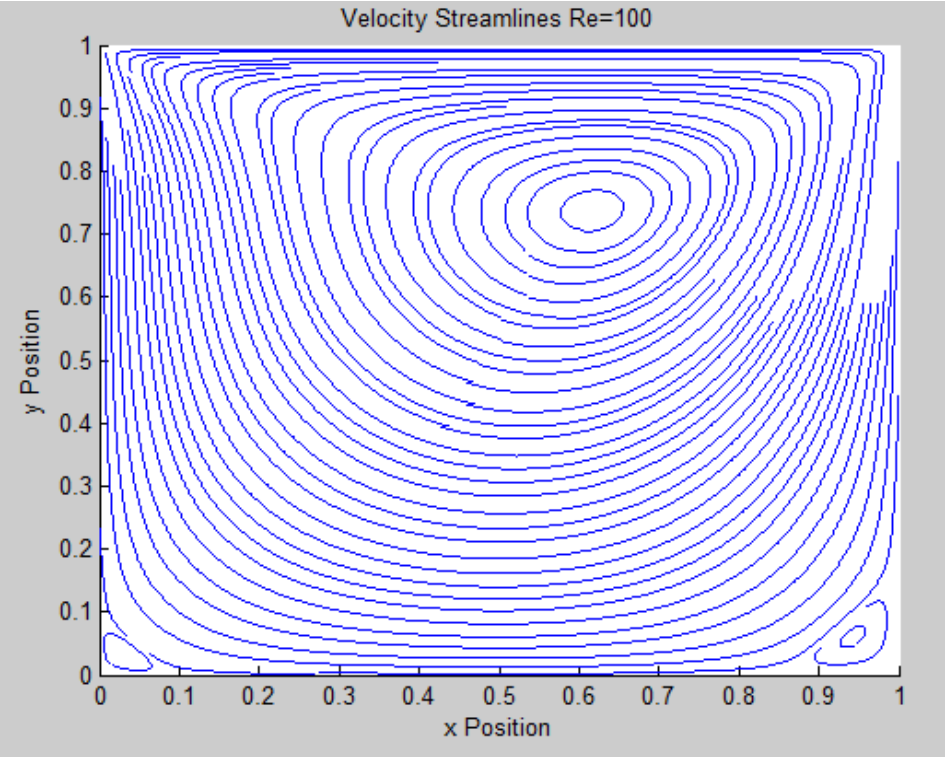

Figure 5.4. Square cavity streamlines, Re=100

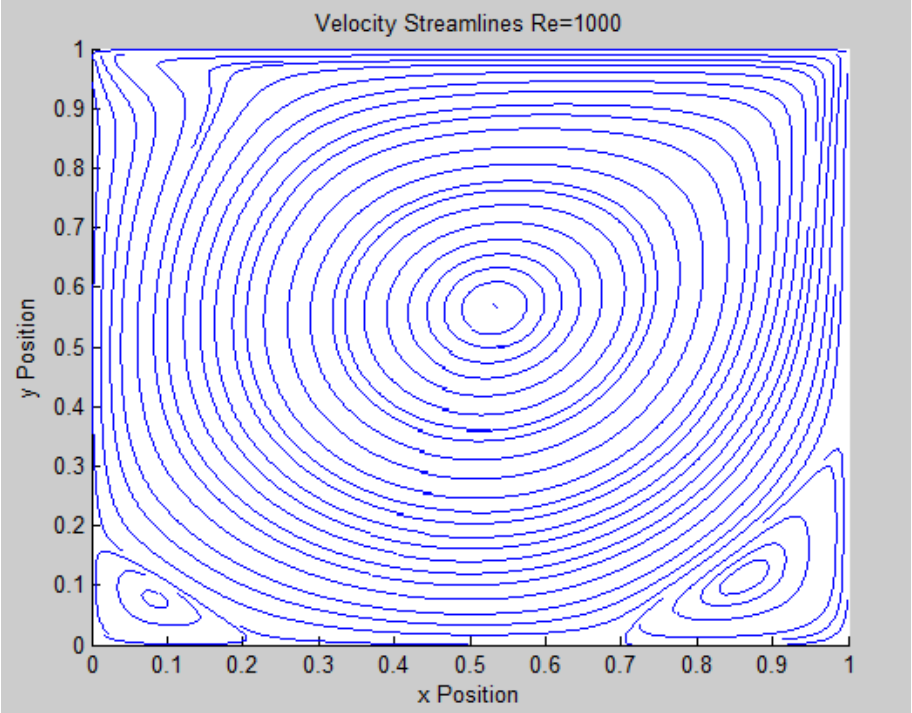

Figure 5.5 Square cavity streamlines, Re=1000

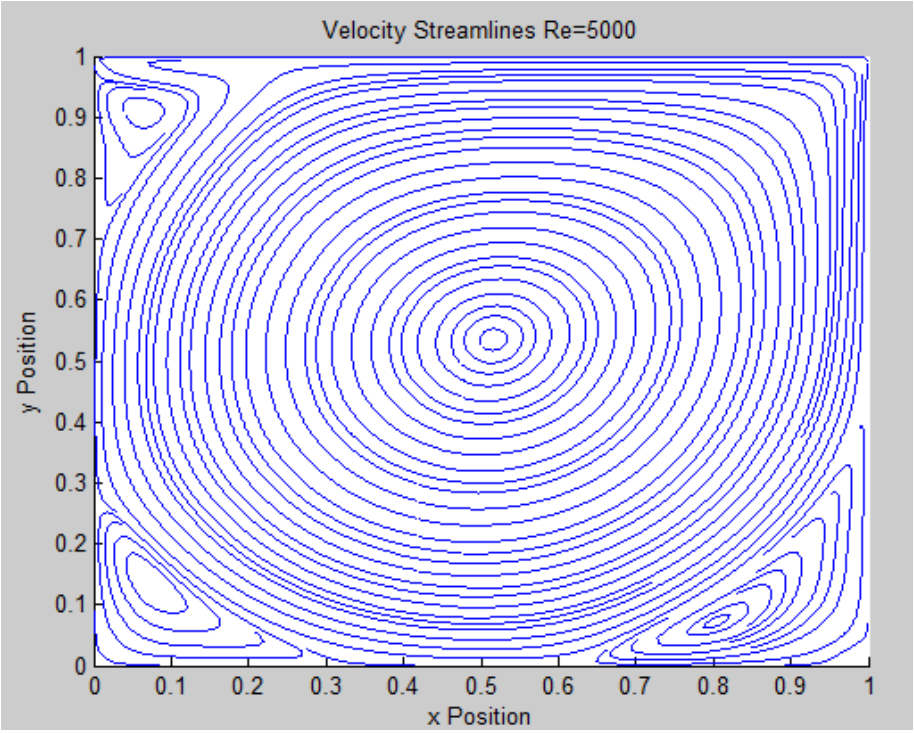

Figure 5.6 Square cavity streamlines, Re=5000

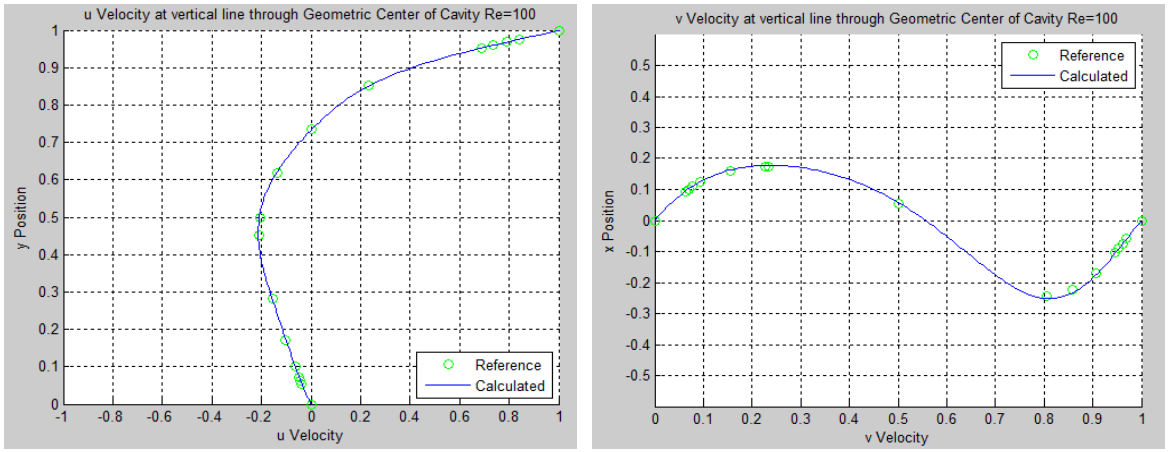

(a)

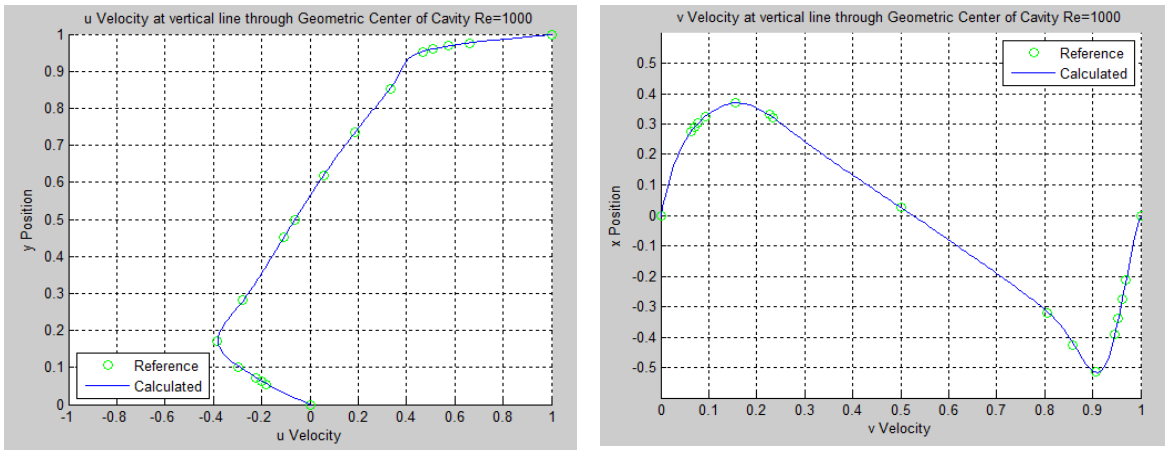

(b)

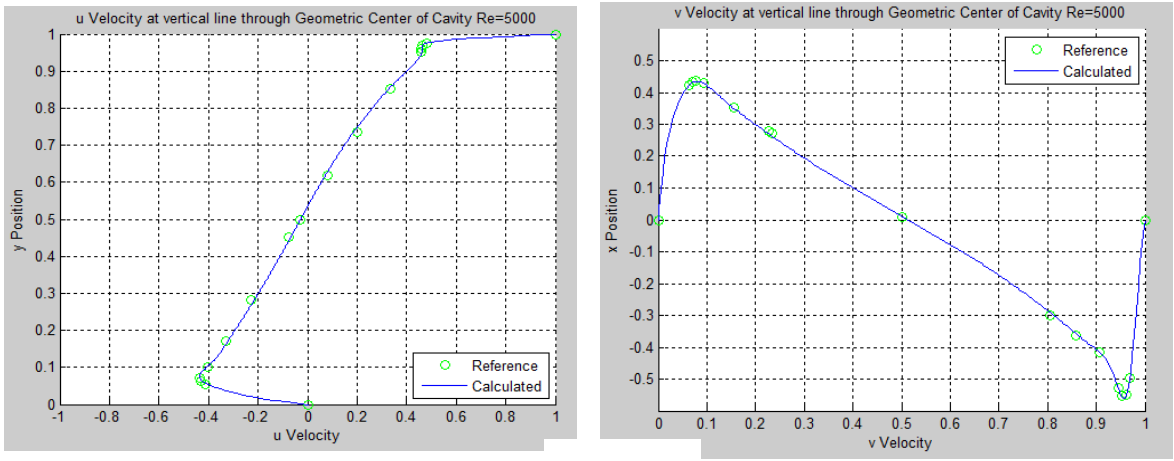

(c)

Figure 5.7. Benchmark comparison. Horizontal velocity (left), Vertical velocity (right)

Re= 100, b) Re=1000, c) Re= 5000

Analysis of the results

	Re=100			
	u-min Reference	16x16 Nodes	32x32 Nodes	64x64 Nodes
	-0.2109	-0.1888	-0.1988	-0.2121
Error %		11.70	6.08	0.565
	v-min Reference	16x16 Nodes	32x32 Nodes	64x64 Nodes
	-0.2453	-0.2289	-0.2371	-0.2518
Error %		7.16	3.45	2.58
	v-max Reference	16x16 Nodes	32x32 Nodes	64x64 Nodes
	0.1753	0.1583	0.1685	0.1779
Error %		10.73	4.03	1.46

Table 5.1. Mesh sizing analysis, Re=100

Figures 5.4 through 5.6 show the streamlines for de different Reynolds numbers. With Re=100, a relatively low number, the cavity features a consistent rotating path with a main eddy located at the top right of the cavity. It can be seen in figure 5.7 a) how for this Reynolds number the maximum horizontal velocity at the middle of the width is located almost mid-height and it has a value close to -0,2. As the Reynolds number is increased to 1000 it is obvious that the flow characteristics are different, but it is more evident for a Re= 5000. For this Reynolds number, the main eddy is located closer to the center of the cavity. In both bottom and top left corners, smaller eddies begin to form. This phenomenon will be recalled in the Insights on turbulence section. Furthermore, it can be noted how the maximum horizontal velocity location at mid-with moved to the bottom part of the cavity. In this case it still has a negative value but the absolute value almost doubled. For all cases, vertical velocities maxima moved closer to the edges of the cavity as the Reynolds number was increased. The reader is invited to review section 3 in the Appendix, where different

comparison tables are used to test the accuracy of the numerical method. In Table 5.1 it is possible to note how the accuracy of the numerical method improves as the mesh size is increased. The present table exemplifies the case of Re=100, but the observed pattern was the same for all Reynolds numbers.

6. Natural convection

Natural convection refers to the type of heat transfer mechanism in which movement is not caused by any external force. Instead, the motion is caused by interactions of gravity and density differences within a fluid (27). These density differences are caused by temperature gradients that can be calculated using the energy equation. This implies that now, for solving natural convection problems, the three main aforementioned equations will be needed: momentum, energy and continuity.

Governing equations

For convenience, the governing equations (continuity, momentum and energy) will be formulated below in Cartesian form.

$$\frac{\partial u}{\partial x}+\frac{\partial v}{\partial y}=0 \qquad \text{(Eq. 6.1)}$$

$$\frac{\partial u}{\partial t}+u\frac{\partial u}{\partial x}+v\frac{\partial u}{\partial y}=-\frac{1}{\rho_0}\frac{\partial p}{\partial x}+\frac{\mu}{\rho_0}\left(\frac{\partial^2 u}{\partial x^2}+\frac{\partial^2 u}{\partial y^2}\right) \qquad \text{(Eq. 6.2)}$$

$$\frac{\partial v}{\partial t}+u\frac{\partial v}{\partial x}+v\frac{\partial v}{\partial y}=-\frac{1}{\rho_0}\frac{\partial p}{\partial y}+\frac{\mu}{\rho_0}\left(\frac{\partial^2 v}{\partial x^2}+\frac{\partial^2 v}{\partial y^2}\right)+g_y-\beta_0 g_y(T-T_0) \qquad \text{(Eq. 6.3)}$$

$$\rho_0 c_p\left(\frac{\partial T}{\partial t}+u\frac{\partial T}{\partial x}+v\frac{\partial T}{\partial y}\right)=k\left(\frac{\partial^2 T}{\partial x^2}+\frac{\partial^2 T}{\partial y^2}\right) \qquad \text{(Eq. 6.4)}$$

The equation of motion in the y direction (Eqn. 71) incorporates the Boussinesq approximation. The spirit of the Boussinesq approximation is to account for the relevant buoyancy forces caused by density gradients (22). The symbol β stands for the volumetric thermal expansion coefficient. In order to simplify the above equations and for an easier understanding of the physical phenomena, the dimensionless form of the equations is presented. The dimensionless characteristic quantities are given below:

$$\check{x}=\frac{x}{l_0}\quad \check{y}=\frac{y}{l_0}\quad \check{t}=\frac{v_0}{l_0}t\quad \check{u}=\frac{u}{u_0}\quad \check{v}=\frac{v}{u_0}\quad \check{T}=\frac{T-T_0}{T_1-T_0} \qquad \text{(Eq. 6.5)}$$

Now that the characteristic quantities have been defined, it is possible to obtain the dimensionless equations. The only thing left is the choice of u_0. According to the information found in transport phenomena literature, the appropriate choice for u_0 for free convection is α/l_0. In this case α is the thermal diffusivity of the fluid.

$$\frac{\partial \check{u}}{\partial x}+\frac{\partial \check{v}}{\partial y}=0 \qquad \text{(Eq. 6.6)}$$

$$\frac{\partial \check{u}}{\partial \check{t}} + \check{u}\frac{\partial \check{u}}{\partial \check{x}} + \check{v}\frac{\partial \check{u}}{\partial \check{y}} = -\frac{\partial \check{P}}{\partial \check{x}} + Pr\left(\frac{\partial^2 \check{u}}{\partial \check{x}^2} + \frac{\partial^2 \check{u}}{\partial \check{y}^2}\right) \quad \text{(Eq. 6.7)}$$

$$\frac{\partial \check{v}}{\partial \check{t}} + \check{u}\frac{\partial \check{v}}{\partial \check{x}} + \check{v}\frac{\partial \check{v}}{\partial \check{y}} = -\frac{\partial \check{P}}{\partial \check{y}} + Pr\left(\frac{\partial^2 v}{\partial x^2} + \frac{\partial^2 v}{\partial y^2}\right) - GrPr^2\check{T} \quad \text{(Eq. 6.8)}$$

$$\left(\frac{\partial \check{T}}{\partial \check{t}} + \check{u}\frac{\partial \check{T}}{\partial \check{x}} + \check{v}\frac{\partial \check{T}}{\partial \check{y}}\right) = \left(\frac{\partial^2 \check{T}}{\partial \check{x}^2} + \frac{\partial^2 \check{T}}{\partial y^2}\right) \quad \text{(Eq. 6.9)}$$

In the above equations Pr stands for the Prandtl number and Gr stands for the Grashof number.

$$Pr = \frac{\nu}{a} \quad \text{(Eq. 6.10)}$$

$$Gr = \frac{g\beta(T_1 - T_0)l_0^3}{\nu^2} \quad \text{(Eq. 6.11)}$$

In the Grashof number ν stands for the kinematic viscosity, β represents the coefficient of thermal expansion and l_o is a characteristic length. The product of the Prandtl and Grashof number is known as the Rayleigh number.

$$Ra = PrGr \quad \text{(Eq. 6.12)}$$

The differentially heated cavity problem

Once the governing equations and working principles of natural convection have been defined, we can proceed with a practical problem:

Consider a two-dimensional flow of a Boussinesq fluid of Prantl 0.71 in a square cavity with the x and y axis defined in the lower left corner of the square. The velocity components in all the boundaries are zero. The cavity is heated on one side with a temperature of 1 (T_h=1). The other side of the cavity is kept with a uniform temperature of 0 (T_c=0). The upper and bottom sides of the cavity behave as adiabatic surfaces. Figure 6.1 shows a schematic

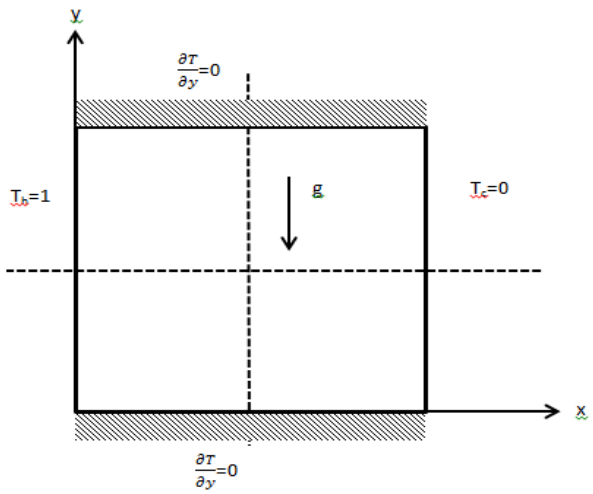

Figure 6.1 Schematic for natural convection

configuration of the problem above.

6.1.1. Deliverables and benchmark solution

In order to check if the numerical solution is accurate, the benchmark values of the velocity field and other parameters were obtained from a previous study (28). The parameters to compare are: the maximum values for vertical and horizontal velocities at the geometric center of the cavities and their location. Also, the average, maximum and minimum Nusselt number in the hot wall of the cavity will be compared with a reference value. Furthermore, the streamlines plot for velocities is also given and compared. The temperature field of the flow in the cavity can be compared as a function of the Rayleigh number. The local Nusselt number in the wall is determined with the following equation:

$$Nu = \int_0^1 \frac{\partial T}{\partial x} dz \qquad \text{(Eq. 6.13)}$$

The previously mentioned results have to be delivered for the following set of Rayleigh numbers: Ra= 1000, Ra=1x10^4, Ra=1x10^5 and Ra=1x10^6. As discussed in the previous section, the Fractional Step Method (FSM) is a reliable technique to solve the continuity equation. The FSM will be used in the resolution of the natural convection problem. Furthermore since the FSM works with an explicit integration scheme, the energy equation will also be worked out in the same fashion. The working principle of the algorithm is the same as in the Lid Driven cavity exercise; the following algorithm shows how after integration they were modified to fit the natural convection exercise. The velocities and temperatures at the faces of their respective control volumes were calculated again using central difference scheme as shown in equation

- *Evaluation of R(u^n)*

(Eq. 6.14)

$$R(u^n) = \frac{1}{\Delta x \Delta y}\left\{-[(u_e u_e - u_w u_w) * \Delta y + (v_n u_n - v_s u_s) * \Delta x] + Pr\left[\frac{u_E - u_P}{\Delta x^2} - \frac{u_P - u_W}{\Delta x^2} + \frac{u_N - u_P}{\Delta y^2} - \frac{u_P - u_S}{\Delta y^2}\right]\right\}$$

(Eqn. 6.15)

$$R(v^n) = \frac{1}{\Delta x \Delta y}\left\{-[(v_n v_n - v_s v_s) * \Delta x + (v_e u_e - v_w u_w) * \Delta y] + Pr\left[\frac{v_E - v_P}{\Delta x^2} - \frac{v_P - v_W}{\Delta x^2} + \frac{v_N - v_P}{\Delta y^2} - \frac{v_P - v_S}{\Delta y^2}\right] + RaPr\frac{T - T_c}{T_h - T_c}\Delta x \Delta y\right\}$$

- *Evaluate up*

$$u^p = u^n + \Delta t\left(\frac{3}{2}R(u^n) - \frac{1}{2}R(u^{n-1})\right) \qquad \text{(Eq. 6.16)}$$

$$v^p = v^n + \Delta t\left(\frac{3}{2}R(v^n) - \frac{1}{2}R(v^{n-1})\right) \qquad \text{(Eq. 6.17)}$$

- *Evaluate $\nabla \cdot u^p$ and solve the discrete Poisson equation*

$$\frac{\tilde{P}_E-\tilde{P}_P}{d_{EP}}\Delta x-\frac{\tilde{P}_P-\tilde{P}_W}{d_{PW}}\Delta x+\frac{\tilde{P}_P-\tilde{P}_N}{d_{PN}}\Delta y-\frac{\tilde{P}_S-\tilde{P}_P}{d_{SP}}\Delta x=\frac{1}{\Delta t}\left(u_e^p\Delta y-u_w^p\Delta y+v_n^p\Delta x-v_s^p\Delta x\right) \quad \text{(Eq. 6.18)}$$

- *Obtain the new velocity field*

$$u^{n+1}=u^p-\Delta t\left(\frac{\tilde{P}_{i-1,j}-\tilde{P}_{i,j}}{\Delta x}\right) \quad \text{(Eq. 6.19)}$$

$$v^{n+1}=v^p-\Delta t\left(\frac{\tilde{P}_{i,j-1}-\tilde{P}_{i,j}}{\Delta y}\right) \quad \text{(Eq. 6.20)}$$

- *Evaluation of R(T^n)*

(Eq. 6.21)

$$R(T^n)=\frac{1}{\Delta x\Delta y}\left\{-[(T_e u_e-T_w u_w)*\Delta y+(v_n T_n-v_s T_s)*\Delta x]+\left[\frac{T_E-T_P}{\Delta x^2}-\frac{T_P-T_W}{\Delta x^2}+\frac{T_N-T_P}{\Delta y^2}-\frac{T_P-T_S}{\Delta y^2}\right]\right\}$$

- *Obtain the new Temperature field*

$$T^{n+1}=T^n+\Delta t\left(\frac{3}{2}R(T^n)-\frac{1}{2}R(T^{n-1})\right) \quad \text{(Eq. 6.22)}$$

The algorithm continues until convergence is achieved. The convergence criterion is shown in equation 5.30. The following figures show the streamline, temperature and velocity plots for the different Rayleigh numbers. For a better appreciation of the outcome of the simulation, the reader is invited to check the comparison tables found in section 3 in the Appendix.

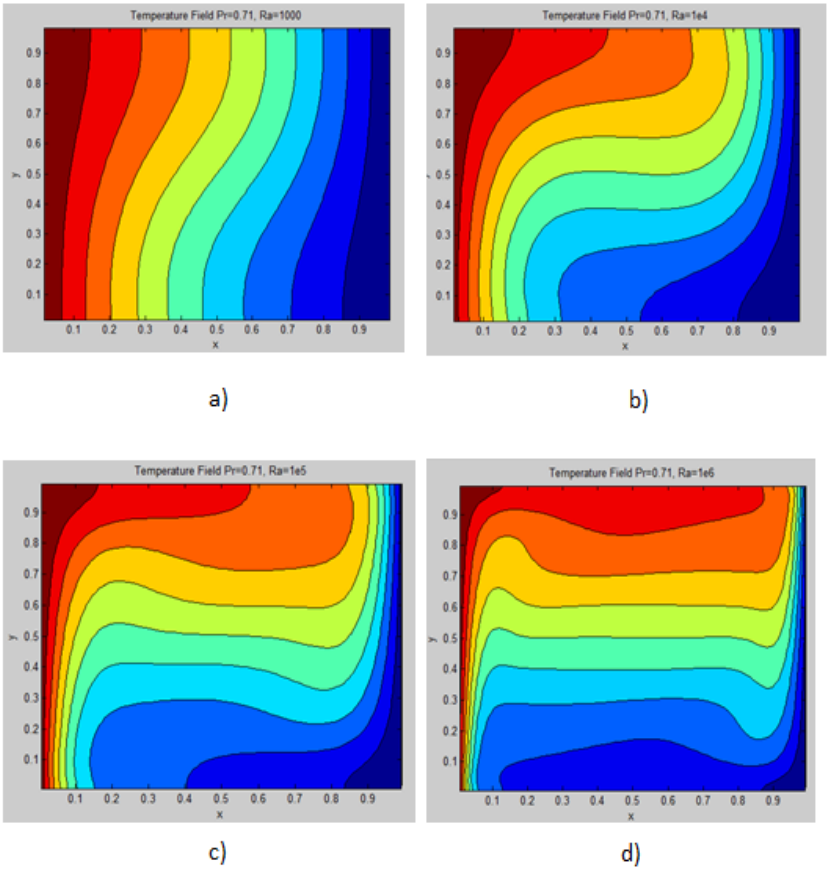

Figure 6.3 Contour maps for Temperature

a.) Pr=0.71, Ra=1x10^3
b.) Pr=0.71, Ra=1 x10^4
c.) Pr=0.71, Ra=1 x10^5
d.) Pr=0.71, Ra=1 x10^6

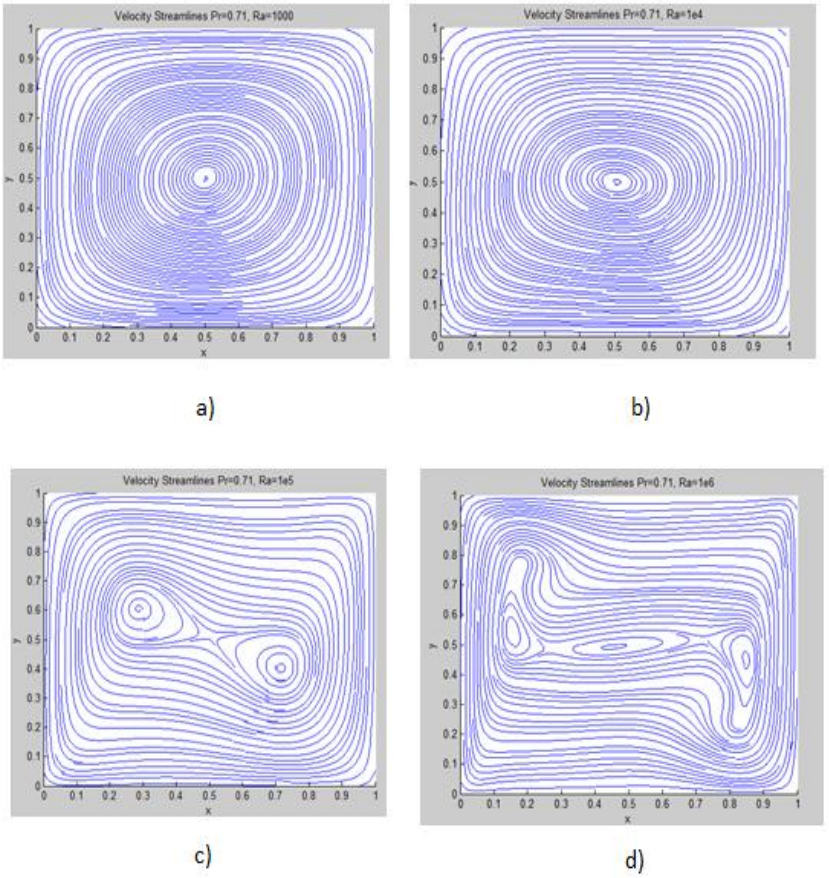

Figure 6.2. Velocity streamlines plot

a.) Pr=0.71, Ra=1 x10^3
b.) Pr=0.71, Ra=1 x10^4
c.) Pr=0.71, Ra=1 x10^5
d.) Pr=0.71, Ra=1 x10^6

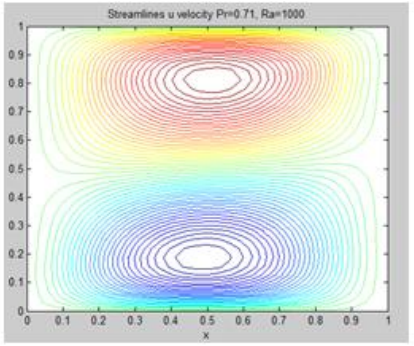

a)

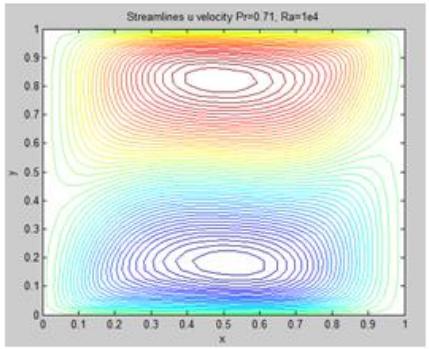

b)

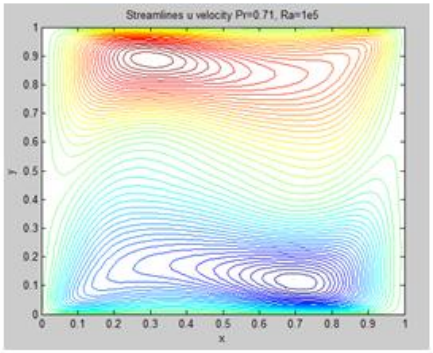

c)

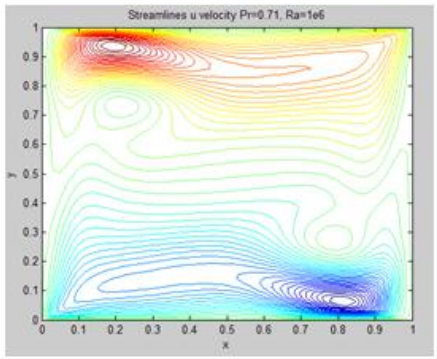

d)

Figure 6.5. Horizontal velocity streamlines

a.) Pr=0.71, Ra=1x10^3
b.) Pr=0.71, Ra=1x10^4
c.) Pr=0.71, Ra=1x10^5
d.) Pr=0.71, Ra=1x10^6

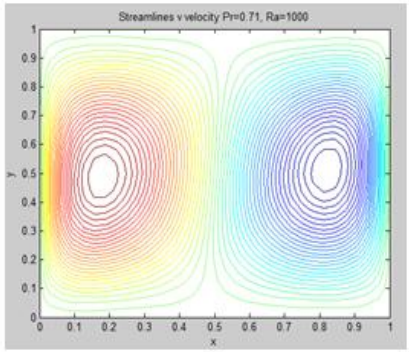

a)

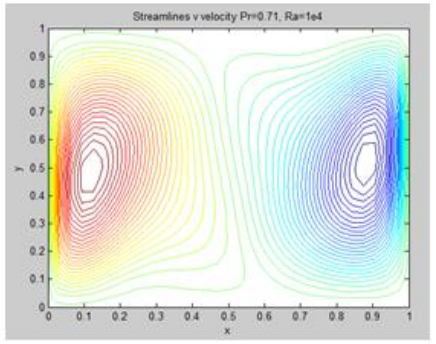

b)

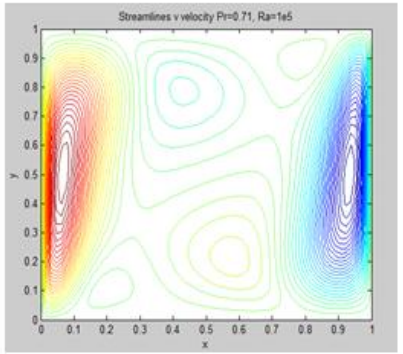

c)

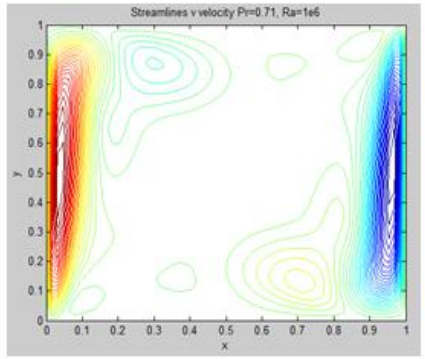

d)

Figure 6.4. Vertical velocity streamlines

a.) Pr=0.71, Ra=1x10^3
b.) Pr=0.71, Ra=1x10^4
c.) Pr=0.71, Ra=1x10^5
d.) Pr=0.71, Ra=1x10^6

Analysis of the results

There are several conclusions to be drawn from the Natural convection problem. Starting from the streamlines, it can be noted that as the previous exercise, for small Rayleigh numbers, the flow is characterized by a single main eddy close to the center of the cavity. At $Ra=1X10^5$, the main eddy breaks into two smaller vortices. As the Rayleigh number is increased, smaller eddies start to appear mainly expanding through the upper-left and bottom-right corners of the cavity. As a result of this behavior, the temperature field is also modified. Mainly, the temperature distribution in small Rayleigh numbers is more equally distributed among the width of the cavity. As Ra increases, the cavity shows a stratified temperature field but this time in the horizontal direction. From the horizontal velocity streamline is possible to see how as Ra increases, the areas of high velocities move towards the corners of the cavity. The same behavior is appreciated in the plot for the vertical velocity. In the section 3 in the Appendix, different comparison tables can be found to check the accuracy of the numerical algorithm. In these tables, the average and maximum Nusselt number found for the problems is also listed. As previously mentioned the Nusselt number is a direct indicator of the heat transfer coefficient and thus of the heat losses. It can be appreciated that as the flow becomes more turbulent, the Nusselt number is also increased in both mean and maximum values.

7. Unstructured finite-volume discretization

In previous sections the discretized transport equations have been solved using the Cartesian coordinate system and rectangular grids. So far, the analysis has been limited to one or two-dimensions, the results have been in good agreement with the benchmark solutions. When dealing with complex shapes, the mesh has to be able to adapt to the geometry of the domain in order to solve accurately the discretized equations. The same applies for a three dimensional analysis. The present section defines and describes the discretization of unstructured meshes.

Theoretical background

Unstructured meshes are characterized with elements with irregular connectivity and a strong information dependency link between neighbor control volumes (25). In two-dimensional analysis, triangular shapes are broadly used in unstructured meshes. For three-dimensions there are several shapes like pyramids, prisms with triangular bases but mainly: tetrahedrons. The figure below shows a typical arrangement of an unstructured mesh in two-dimensions and a common tetrahedral element.

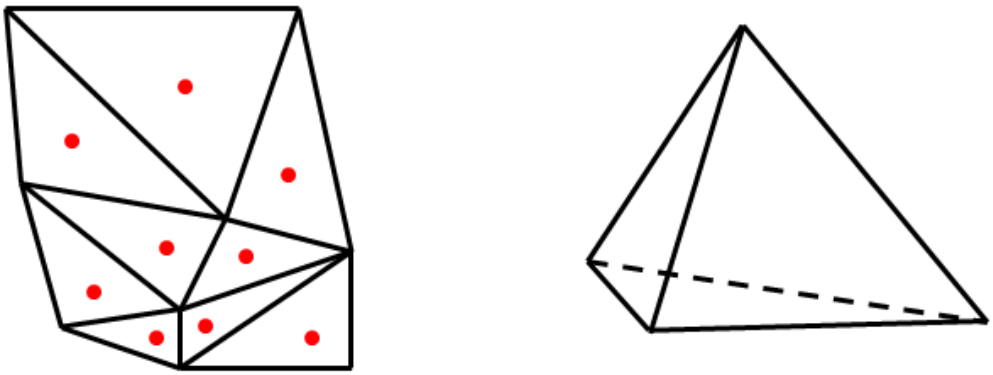

Figure 7.1. Unstructured mesh arrangement 2D (Left), Tetrahedron (Right)

In order to proceed with the discretization in an unstructured mesh, it is necessary to come back to the standard transport equation:

$$\frac{\partial(\rho\phi)}{\partial t} + \nabla \cdot (\rho\vec{u}\phi) = \nabla \cdot (\Gamma\nabla\phi) + S \qquad \text{(Eq. 7.1)}$$

When this equation is integrated over a general control volume and using an explicit scheme, the result is the following (29):

(Eq. 7.2)

$$\int \frac{(\rho\phi)^{n+1} - (\rho\phi)^n}{\Delta t} dV + \int \nabla \cdot (\rho\vec{u}\phi)^n dV = \int \nabla \cdot (\Gamma \nabla\phi)^n \, dV + \int S^n dV$$

(Eq. 7.3)

$$\frac{(\rho\phi)^{n+1} - (\rho\phi)^n}{\Delta t} V_c + \sum_f \left(\rho_f \overrightarrow{u_f} \phi_f\right)^n \cdot \overrightarrow{n_f} A_f = \sum_f \left(\Gamma_f \nabla\phi_f\right)^n \cdot \overrightarrow{n_f} A_f + S^n V_c$$

In the above equations, f, stands for the cell face. $\overrightarrow{n_f}$ and $A_f$represent the face normal vector and face area. The next step in the treatment is to know how to treat the convective and diffusive terms. The approximation of the convective term is presented in the equation below:

(Eq. 7.4)

$$C = \sum_f \left(\rho_f \overrightarrow{u_f} \phi_f\right)^n \cdot \overrightarrow{n_f} A_f = \sum_f \dot{m}_f \phi_f$$

As it can be seen, the convective term is approximated with a summation of the mass flow multiplied times the variable of interest ϕ_f. In order to approximate the value of ϕ_f in the face, it is necessary to use a numerical scheme. For simplicity only the previously addressed upwind scheme will be described with reference to the node locations shown in figure 7.2.

$\phi_f = \phi_P \qquad \dot{m}_f \geq 0$ (Eq. 7.5)

$\phi_f = \phi_F \qquad \dot{m}_f \leq 0$

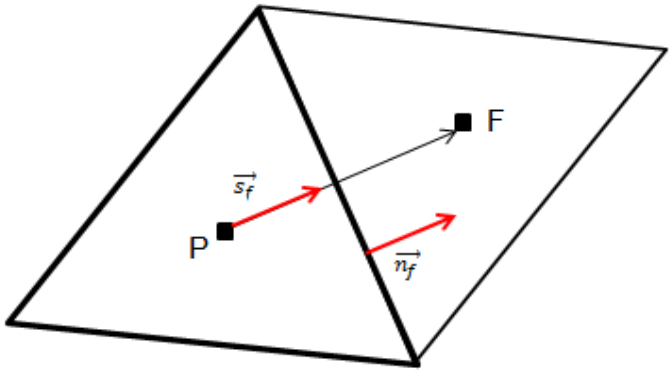

Figure 7.2. Node position for unstructured mesh

Now, the task is to perform the discretization of the diffusion term. The challenge, as can be seen in equation 7.3, the diffusion term features a gradient evaluation in the face of the control volume. In this work, the diffusive term will be evaluated using the Direct Gradient Evaluation criterion (29).

(Eq. 7.6)

$$D = \sum_f \left(\Gamma_f \nabla\phi_f\right)^n \cdot \overrightarrow{n_f} A_f = \sum_f \Gamma_f \frac{\phi_{F'} - \phi_{P'}}{d_{PF}} A_f^s \qquad A_f^s = A_f / \left(\vec{s}_f \cdot \vec{n}_f\right)$$

The unstructured convection-diffusion problems

Once the convection-diffusion equation has been discretized, it is possible to try the new resolution method with two examples (29). These examples were solved using TERMOFLUIDS software.

Case 1: Square box with Dirichlet boundary condition at yz planes and Neumann boundary conditions at the other planes, $\frac{\partial\phi}{\partial x}$ and $\frac{\partial\phi}{\partial x}$. Figures 7.3 and 7.4 show the solution of the problem in structured and unstructured mesh respectively. It can be seen that the distribution of the variable ϕ over the control volume is very similar.

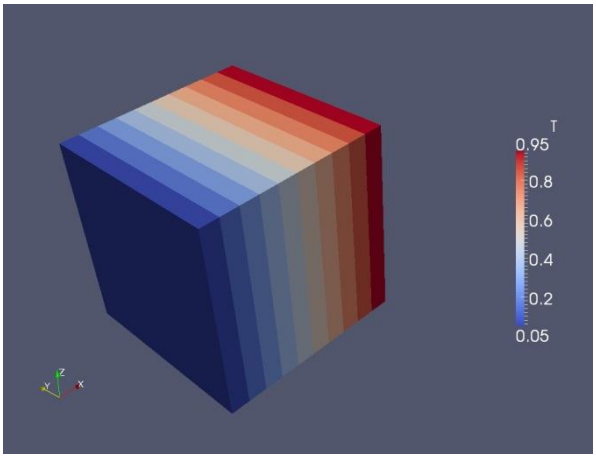

Figure 7.3. Structured diffusion problem

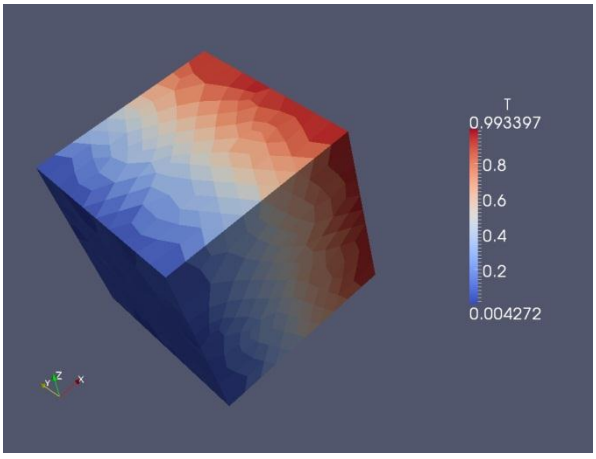

Figure 7.4. Unstructured diffusion problem

Case 2: The second problem to be solved has already been addressed in a two-dimensional form in the convection-diffusion resolution section. It is commonly known as the Smith-Hutton problem and the geometry is the following: rectangular box with, Lx=2, Ly=Lz=1. The boundary conditions are given in Table 7.1. The value of Alfa in the boundary conditions is 10. The velocity field is given by equations 37 and 38:

$$u(x,y) = 2y(1-x^2) \quad \text{(Eq. 7.7)}$$

$$v(x,y) = -2x(1-y^2) \quad \text{(Eq. 7.8)}$$

Table 7.1. Boundary conditions for the Smith-Hutton problem

Boundary Condition	Position	
ϕ=1-tanh(α)	x =-1	0<y<1
ϕ=1-tanh(α)	-1<x<1	y=1
ϕ=1-tanh(α)	x =1	0<y<1
$\frac{\partial \phi}{\partial y} = 0$	0<x<1	y=0
ϕ =1+tanh((2x+1)α)	-1<x<0	y=0

The following figure shows the results of the problem for a Péclet number of 1000. The reader is invited to compare the flow field with the result of the two dimensional situation shown in figure 4.11.

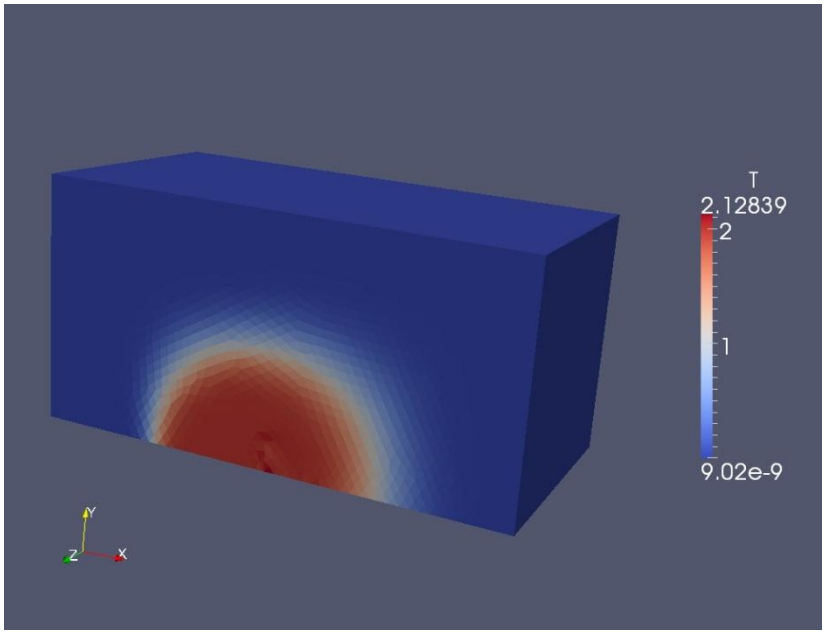

Figure 7.5. Smith-Hutton unstructured problem

Analysis of the results

It is possible to see from figure 7.4 that both results are in good agreement for structured and unstructured meshes. Both cases featured a transient state where the convergence criteria were set as the difference between iterations had to be smaller than $1x10^{-6}$. In figures 7.4 and 7.5 is possible to see some slight differences in the maximum and minimum values for the color palette of the curves. It is suspected that these differences arise from the use of the plotting software and not the numerical algorithm. As previously mentioned, the results of this simulation were in good agreement with the two-dimensional results of the Smith-Hutton problem described in section 4.

8. Insights on turbulence

So far the analysis of fluid dynamics has been performed on laminar flows. However most phenomena encountered on a daily basis in engineering problems deals with turbulent flows. This section deals with some turbulent flow topics such as scales of motion, energy cascade, symmetry preservation and time averaging.

Introduction

Studies have shown that the nature of turbulence is irregular, random and chaotic (29). This makes the study of turbulence flows a complex, challenging and still developing task. However one of the motivations to study turbulent flow is that allows for a better transport and flow mixing. The transport equations previously mentioned are capable of describing the motion of turbulent flows; however, the computational effort is increased dramatically. It is so because the Navier-Stokes equations solve all the relevant length and time scales. It is possible to characterize a flow using a well-known and previously mentioned non-dimensional parameter: The Reynolds number:

$$Re = \frac{\rho V L}{\mu} \qquad \text{(Eq. 8.1)}$$

Depending on the value of Re, the flow can be characterized as: Laminar, Transitional or Turbulent.

Scales of motion and Energy Cascade

At high Reynolds number, when the flow is turbulent, it is possible to identify several scales. The large scales are strongly dependent on the main flow and boundary conditions. The small scales however behave according to the energy rate they receive and the energy dissipation due to viscosity. It is implied that the small scales are independent of the main flow geometry and their behavior can be generalized. According to Richardson (30), turbulence can be regarded as a composition of different eddies. These eddies vary in size and are defined as turbulent motion. Large eddies are unstable and disintegrate, transferring their kinetic energy to smaller eddies. In turn, these eddies go through the same process into smaller scales until eventually their Reynolds number becomes small enough that molecular viscosity starts dissipating kinetic energy. This dissipation process at low scale converts kinetic energy into thermal energy. In his work ‘The local structure of turbulence in incompressible viscous fluid for very large Reynolds numbers’ (31), Kolmogorov proposes some hypothesis regarding the characterization of scales of motion. The first hypothesis suggests that at high Reynolds number, the small scales are isotropic. The second

hypothesis says that the statistics of small scales only depend on the dissipation rate (ε) and the kinematic viscosity (ν):

$$\eta \equiv (\nu^3/\varepsilon)^{1/4} \quad \text{(Eq. 8.2)}$$

$$u_\eta \equiv (\varepsilon\nu)^{1/4} \quad \text{(Eq. 8.3)}$$

$$\tau_\eta \equiv (\nu/\varepsilon)^{1/2} \quad \text{(Eq. 8.4)}$$

Equation 8.2, 8.3 and 8.4 show the Kolmogorov length, velocity and time microscales. The third Kolmogorov hypothesis suggests that according to the size of the eddies, several ranges can be identified as shown in figure 8.1:

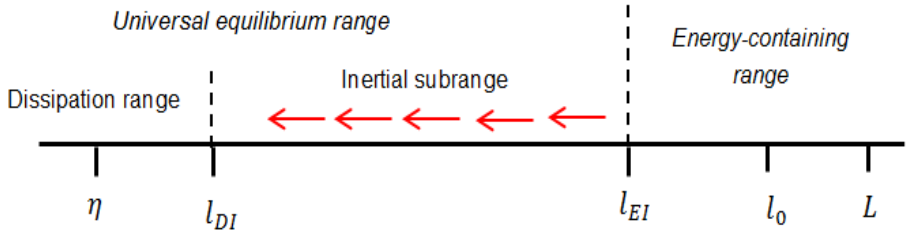

Figure 8.1 Eddy sizes showing lengthscales and ranges

The energy spectrum and Burger's equation

The next step is to figure out how the kinetic energy is distributed among the length scales. In order to do so a useful concept to introduce is the wavenumber spectrum in Fourier mode:

$$e^{i\kappa\cdot x} = \cos(\kappa \cdot x) + i\,\sin(\kappa \cdot x) \quad \text{(Eq. 8.5)}$$

The previous equation is a sinusoidal function with a wavelength:

$$l = \frac{2\pi}{\kappa} \quad \text{(Eq. 8.6)}$$

κ is a symbol that represents a wavenumber or Fourier coefficient. The total kinetic energy of a flow is defined as the integration of the energy contained in all the wavenumbers from zero to infinite:

$$k = \int_0^\infty E(\kappa)\, d\kappa \quad \text{(Eq. 8.7)}$$

The following figure shows the energy as a function of the wave number κ. From it, it is possible to identify the same ranges as in figure 8.1: Energy containing range, inertial sub range and dissipation range.

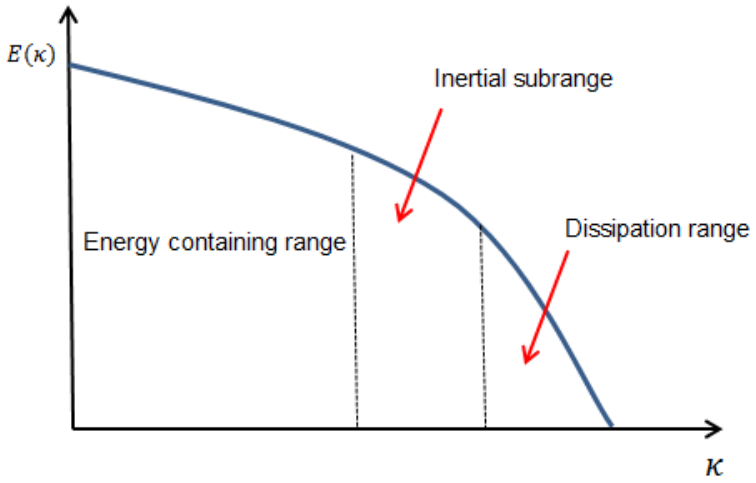

Figure 8.2 Energy spectrum as a function of wavenumbers

Once the energy spectrum plot has been obtained, it is time to continue with the analysis but now introducing the Navier-Stokes and continuity equations.

$$\frac{\partial \boldsymbol{u}}{\partial t} + (u \cdot \nabla)u = \frac{1}{Re}\Delta u - \nabla p \qquad \text{(Eq. 8.8)}$$

$$\nabla \cdot u = 0 \qquad \text{(Eq. 8.9)}$$

In order to simplify the analysis of the previous equations, the Burgers equation is introduced. This equation can be used to model specific patterns of flow behavior. The presented Burgers equation is one dimensional and it resembles and features many aspects of the Navier-Stokes equations.

$$\frac{\partial u}{\partial t} + u\frac{\partial u}{\partial x} = \frac{1}{Re}\frac{\partial^2 u}{\partial x^2} + f \qquad \text{(Eq. 8.10)}$$

The analysis continues with the transformation of Burgers equation into a Fourier mode. The transformation of terms from the Burgers equation into Fourier space is the following:

Transient term: (Eq. 8.11)

$$\frac{\partial u}{\partial t} = \sum_{-N}^{+N} \left(\frac{\partial \hat{u}_k}{\partial t} \right) e^{ikx}$$

Diffusive Term (Eq. 8.12)

$$\frac{\partial^2 u}{\partial x^2} = \sum_{-N}^{+N} -k^2 \, \hat{u}_k e^{ikx}$$

External Forces (Eq. 8.13)

$$f = \sum_{-N}^{+N} F_k \, e^{ikx}$$

Convective Term (Eq. 8.14)

$$u \frac{\partial u}{\partial x} = \sum_{p=-N, q=-N}^{p=+N, q=+N} \hat{u}_p \, iq \hat{u}_q e^{i(p+q)x}$$

Since it is possible to solve each Fourier coefficient separately, the Burgers equation now reads:

(Eq. 8.15)

$$\frac{\partial \hat{u}_k}{\partial t} + \sum_{k=p+q} \hat{u}_p iq \hat{u}_q e^{i(p+q)x} = -\frac{k^2}{Re} \hat{u}_k + F_k$$

When the velocity $\hat{u}_k$ is multiplied by its complex conjugate, the result is the kinetic energy transport E_k, previously defined in equation 8.7. The equation for the kinetic energy transport is the following:

$$\frac{\partial E_k}{\partial t} = -\frac{2k^2}{Re} E_k - \left(\overline{\hat{u}_k} \, C_k(\hat{u}_p, \hat{u}_q) + \hat{u}_k \overline{C_k(\hat{u}_p, \hat{u}_q)} \right) + \overline{\hat{u}_k} F_k + \hat{u}_k \overline{F_k} \quad \text{(Eq. 8.16)}$$

In the above equation the symbol $\overline{(\cdot)}$ stands for the complex conjugate and the convective and diffusive term are given by:

(Eq. 8.17)

$$C_k(\hat{u}_p, \hat{u}_q) \equiv \sum_{k=p+q} \hat{u}_p i \hat{u}_q$$

$$D = -\frac{2\kappa^2}{Re}\widehat{u_k} \qquad \text{(Eq. 8.18)}$$

The Burgers equation problem

With the former theoretical background now we turn our attention into solving an actual problem involving the Burgers equation. The Burgers equation will be solved using a Reynolds number of 40. On the other hand the initial condition for the velocity is $\hat{u}_k = k^{-1}$. The mode k=0 does not interact with other modes, therefore is assumed $\hat{u}_0 = 0$. It is desired to plot the kinetic energy as a function of the mode for N=20 and N=100 (DNS solution).

The aim of the problem is to find a steady state solution to the kinetic energy equation in Fourier's space. With the boundary conditions it is possible to calculate the velocity $\hat{u}_k$ for the different modes (κ), and then multiply it times its complex conjugate to obtain the kinetic energy. Since the goal is to find a steady state solution, the problem will be solved iteratively until convergence is achieved. The convergence criteria value is taken as $1x10^{-6}$. The integration is performed using a fully explicit scheme with the following time step condition:

(Eq. 8.19)

$$\Delta t = C_1 \frac{Re}{N^2}$$

The value of C_1 is to be examined and discussed afterwards. The convective part, presented in equation 8.15, has an imaginary part. This term has to be updated every iteration considering all the different combinations for the current mode κ. For instance if the current mode is 2, the following combinations for p and q need to be taken into account: (20, -18), (19,-17), (18,-16)…(0,2). The results were plotted and can be appreciated in figure 8.3.

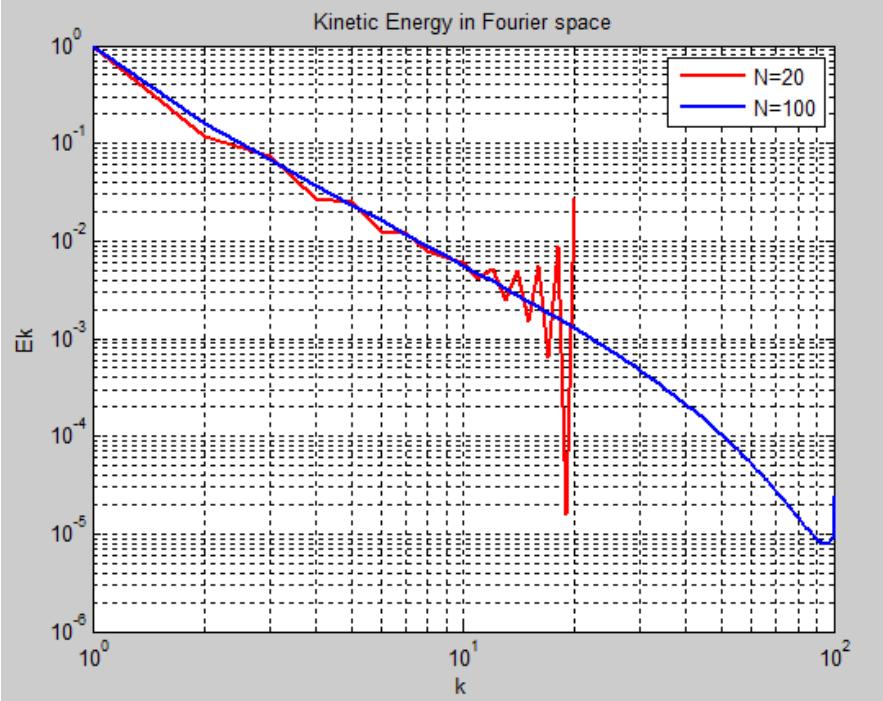

Figure 8.3. Energy spectrum of the steady state solution of Burgers equation

Figure 8.3 features two curves, one where only 20 Fourier modes were taken into account and the other one with 100 elements (DNS solution). It can be seen from the previous figure that the energy spectrum considering only 20 Fourier modes is unstable and is not an accurate representation of the DNS. In order to prevent this, a Large Eddy Simulation is implemented. The spectral eddy viscosity model is proposed (32), it can be applied in Fourier space and it assumes certain properties of the energy spectrum. For the previous example ν =Re^{-1}, now this value will be changed by $\nu_{eff}(k) = \nu + \nu_t(k)$. The k dependant viscosity is defined in the following way:

$$\nu_t\left(\frac{k}{k_N}\right) = \nu_t^{+\infty}\left(\frac{E_{kN}}{k_N}\right)^{1/2}\nu_t^*\left(\frac{k}{k_N}\right) \quad \text{(Eq. 8.20)}$$

$$\nu_t^{+\infty} = 0.31\frac{5-m}{m+1}\sqrt{3-m}C_k^{-3/2} \quad \text{(Eq. 8.21)}$$

$$\nu_t^*\left(\frac{k}{k_N}\right) = 1 + 34.5e^{-3.03\left(\frac{k_N}{k}\right)} \quad \text{(Eq. 8.22)}$$

In the above equations, m stands for the slope of the energy spectrum: in this case 2. C_k in the Kolmogorov constant and it will be plotted with the values of 0.4523 and 0.05 as shown in the following figures.

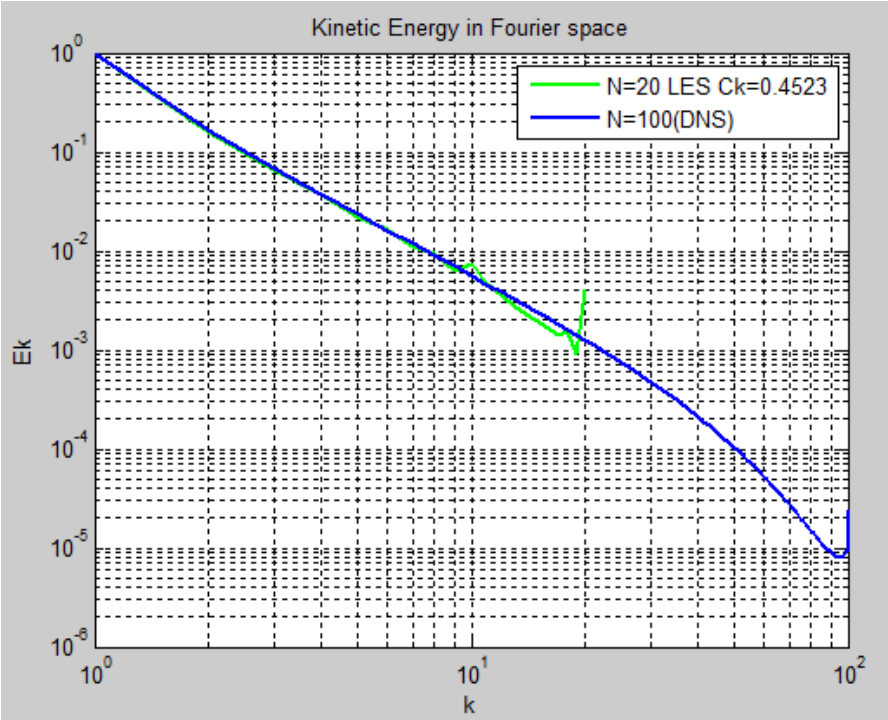

Figure 8.4. Energy spectrum with LES, Ck = 0.4523

As a conclusion for the energy spectrum section is important to mention the role of the different terms in the Burgers equation. The diffusive term (Eqn. 8.18) is dampening energy, especially in the small scales; it does not transport energy at all. On the other hand the convective term (Eqn. 8.17), transports energy, mainly from large to small scales.

Symmetry-preserving discretization

As we have stated before, the Navier-Stokes equations are solved using a fundamental assumption: the domain can be considered as a continuum. However, during the discretization process the domain is divided into smaller elements. It is evident that something must be done in order to preserve certain properties inherited from the continuous equation. Mainly as stated in the previous section, the diffusive term necessarily has to dissipate energy while the convective term and pressure gradient should not contribute to the energy balance. Equation 8.23 shows a finite volume discretization equation:

$$\Omega_s \frac{\partial u_s}{\partial t} + C(u_s)u_s + Du_s + \Omega_s G p_c = 0_s \quad \text{(Eq. 8.23)}$$

$$Mu_s = 0_c \quad \text{(Eq. 8.24)}$$

In the above equation, Ω_s is a diagonal matrix with the sizes of the control volumes. C and D are the convective and diffusive operators respectively. G stands for the gradient operator while M is the integral of the divergence operator. In order to assure that fundamental properties are transferred to the discrete equations, having a stable system and an accurate global kinetic energy balance the following conditions must be true:

- The convection matrix $C(u_s)$ is skew symmetric: diagonal terms null, all other terms symmetric with different sign.
- The diffusive operator D should be positive definite and symmetric
- The gradient and divergence operators should be related in the following way:
  $G = -\Omega_s^{-1} M^*$ (Eqn. 8.25)

If a code complies with the previous conditions it can be regarded as stable and with an accurate kinetic energy balance regardless of the mesh coarseness. While as background theory a matrix notation is useful, a more practical approach to determine symmetry preservation is presented.

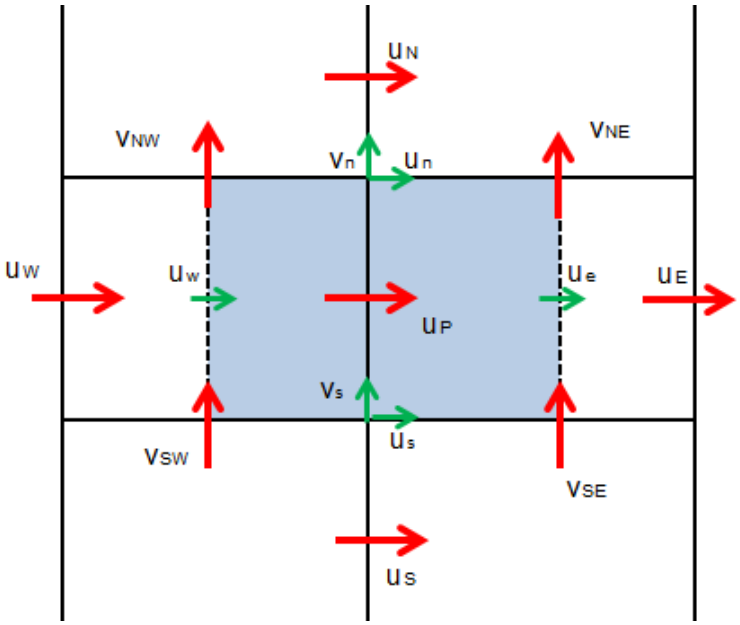

Figure 8.5. Horizontal velocity control volume

If we integrate the convective term from the Navier-Stokes equation over the horizontal control volume shown in the previous figure the result is the following:

(Eq. 8.26)

$$-\int \nabla \cdot (uu) = -\int (uu)_e + \int (uu)_w - \int (uv)_n + \int (uv)_s = -u_e f_e + u_w f_w + -u_n f_n + u_s f_s$$

The face velocities are approximated by a mid-point interpolation, regardless of the arrangement of the mesh.

(Eq. 8.27)

$$-\int \nabla \cdot (uu) = -\frac{1}{2}(u_P + u_E) f_e + \frac{1}{2}(u_P + u_W) f_w + -\frac{1}{2}(u_P + u_N) f_n + \frac{1}{2}(u_P + u_S) f_s$$

Rearranging the previous equation gives:

$$-\int \nabla \cdot (uu) = u_p \frac{-f_e + f_w - f_n + f_s}{2} + u_E \frac{-f_e}{2} + u_W \frac{f_w}{2} + u_N \frac{-f_n}{2} + u_S \frac{f_s}{2} \quad \text{(Eq. 8.28)}$$

Now it is possible to know the matrix coefficients related with the position p

$$C[u]_p = c_P u_P + c_E u_E + c_W u_W + c_N u_N + c_S u_S \quad \text{(Eq. 8.29)}$$

The matrix entries are:

(Eq. 8.30)

$$c_P = \frac{-f_e + f_w - f_n + f_s}{2}$$

$$c_E = \frac{-f_e}{2}$$

$$c_W = \frac{f_w}{2}$$

$$c_N = \frac{-f_n}{2}$$

$$c_S = \frac{f_s}{2}$$

The c_p coefficient makes reference to the value located in the main diagonal on the convective matrix. Since the flux values for the faces (f) are also calculated through a mid-point interpolation, the c_p coefficient is arranged as seen the equation below:

$$c_P = \frac{1}{4}(-f_P + f_W - f_{NW} + f_{SW}) + \frac{1}{4}(-f_E + f_P - f_{NE} + f_{SE}) \quad \text{(Eq. 8.31)}$$

As seen from the equation 8.31, if the coefficient c_p is numerically close to zero for all the velocity control volumes, it can be said that the diagonal of the convective matrix is null.

The off-diagonal symmetry of the matrix is evaluated with the following expression for the control volumes sharing faces:

$$c_{E\,i,j} = -c_{W\,i+1,j} \qquad \text{(Eq. 8.32)}$$

$$c_{N\,i,j} = -c_{S\,i,j+1}$$

If the conditions described in equation 8.32 are met and the coefficients c_p in equation 8.31 are zero, the convective matrix is said to be skew-symmetric.

The evaluation of the diffusive term is carried out performing the integration in a different way as the convective term. It was found that the matrix coefficients only depend on the geometry of the mesh. However, the way to build the off diagonal matrix terms is similar. In that case, the coefficients have to comply with the condition:

$$c_{E\,i,j} = c_{W\,i+1,j} \qquad \text{(Eq. 8.33)}$$

$$c_{N\,i,j} = c_{S\,i,j+1}$$

The coefficients need to have the same sign (positive) so the matrix can be considered as positive definite and symmetric. This condition has to be met even if the mesh is not uniform.

Post processing of turbulence results

Since turbulence is a chaotic and random phenomenon, several different post simulation analysis have to be performed. Before describing the techniques, it is important to settle some important statistics definitions. The turbulent velocity field $U(x,t)$ can be expressed through Reynolds decomposition:

$$U(x,t) = \langle U(x,t) \rangle + u(x,t) \qquad \text{(Eq. 8.34)}$$

The first term in the right hand side of equation 120 makes reference to the mean velocity field, the term on its right it's the velocity fluctuation.

The mean velocity field is defined as:

(Eq. 8.35)

$$\langle U \rangle = \int_{-\infty}^{\infty} V f(V) dV$$

In the previous equation f(V) makes reference to the probability density function (PDF). However, the velocity in a turbulent flow is regarded as random and its PDF is unknown. With the post processing analysis, the average values for velocity and other variables, such as temperature or heat transfer coefficients will be estimated without taking into account the PDF. Since in turbulence the flow will never reach a fully steady state, calculating the process is somehow troublesome. There are several methods to evaluate the mean of a velocity field, here, the time average method is discussed.

The time average method consists in reaching a statistically stationary state (SST). It is said that one flow is in SST when all its statistics remain constant in time. This state can be achieved when the boundary conditions are constant. In order to estimate the mean of a variable in time, the following equation is used:

(Eq. 8.36)

$$\langle U(t)\rangle_{t_0}^{t_0+\Delta T} = \frac{1}{\Delta T}\int_{t_0}^{t_0+\Delta T} U(t')dt'$$

The main questions to be answered are: when the flow can be considered as having reached SST? And, how long the integration period should be (ΔT)? Addressing the previous questions requires a large amount of information storage since it would have to be performed every time step. Instead, it is possible to use partial integrals for each variable of interest (u).

(Eq. 8.37)

$$\tau\langle u\rangle_i^{i+1} = \int_{t=i\tau}^{t=(i+1)\tau} u\,dt$$

In the above equation, τ represents the length in time of each segment. It has to be smaller than the whole integration period but long enough that the number of segments stored is within an acceptable limit. A key feature of the partial integrals is that it is possible to combine them in order to get an estimation of the statistically steady average value.

$$2\tau\langle q\rangle_{i\tau}^{(i+2)\tau} = \tau\langle q\rangle_i^{i+1} + \tau\langle q\rangle_{i+1}^{i+2} \quad \text{(Eq. 8.38)}$$

The simulation is run over a set of time. Each determined period of time, estimation of partial integrals is stored for each significant variable in the simulation. At the end of N segments, the time integrals are combined into sub averages starting from the end of the simulation. The results are then plotted and three stages in the simulation can be identified in the figure below:

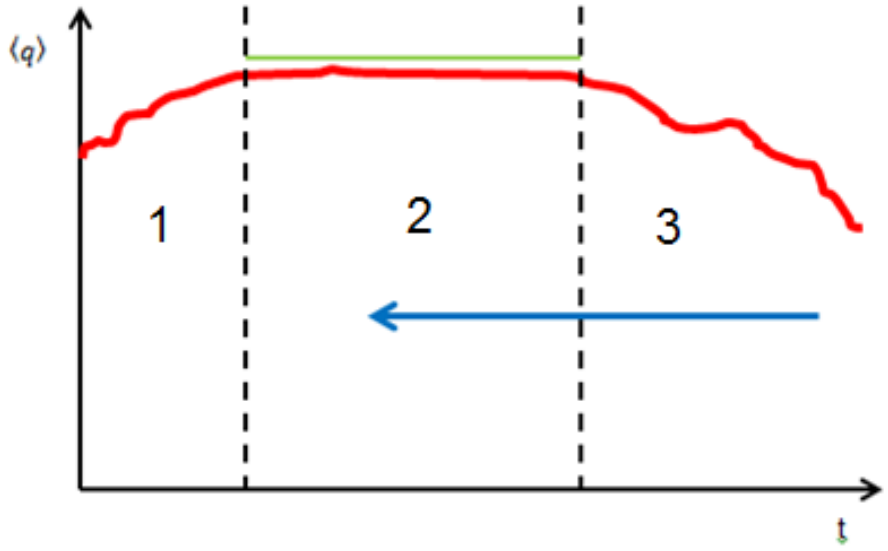

Figure 8.6. Time averaging plot

The previous figure shows the three different stages often encountered in time integration plots. Zone 3 represents the last values of the partial integrals; it indicates that the integration period is too short. Zone 2, shows a set of stable values where only small changes can be identified. Zone 1 may or may not appear on the plot depending the amount of time blocks used in the estimation of the average.

All the previous insights on turbulence will be applied in a practical exercise on natural convection.

Direct numerical simulation of two-dimensional turbulent natural convection flow (33)

The main task of this exercise is to show how the resolution algorithm for handling natural convection is modified in order to adapt to turbulent flows. Even though turbulence is a phenomenon in three-dimensions, the following analysis will be used as a preliminary study in 2D. As a first step, the sections for storing time integrals and check continuity were implemented. The description of the problem is the following: an incompressible Newtonian fluid with Pr = 0.71, is enclosed within a cavity of width L_x=1 and height L_y=4. The fluid has a kinematic viscosity ν, a thermal diffusivity α and can be characterized with the Boussinesq

approximation. The governing equations in primitive variables are the same as the used in the previous natural convection exercise:

$$\frac{\partial \check{u}}{\partial x} + \frac{\partial \check{v}}{\partial y} = 0 \qquad \text{(Eq. 8.39)}$$

$$\frac{\partial \check{u}}{\partial \check{t}} + \check{u}\frac{\partial \check{u}}{\partial \check{x}} + \check{v}\frac{\partial \check{u}}{\partial \check{y}} = -\frac{\partial \check{P}}{\partial \check{x}} + Pr\left(\frac{\partial^2 \check{u}}{\partial \check{x}^2} + \frac{\partial^2 \check{u}}{\partial \check{y}^2}\right) \qquad \text{(Eq. 8.40)}$$

$$\frac{\partial \check{v}}{\partial \check{t}} + \check{u}\frac{\partial \check{v}}{\partial \check{x}} + \check{v}\frac{\partial \check{v}}{\partial \check{y}} = -\frac{\partial \check{P}}{\partial \check{y}} + Pr\left(\frac{\partial^2 v}{\partial x^2} + \frac{\partial^2 v}{\partial y^2}\right) - GrPr^2\check{T} \qquad \text{(Eq. 8.41)}$$

The reference time, velocity and temperature used in the dimensionless form are:

$$\hat{t} = \left(\frac{L_y^2}{\alpha}\right)Ra^{-0.5} \qquad \hat{u} = \left(\frac{\alpha}{L_y}\right)Ra^{-0.5} \qquad \hat{T} = \Delta T \qquad \text{(Eq. 8.42)}$$

A schematic of the problem can be seen in the figure below:

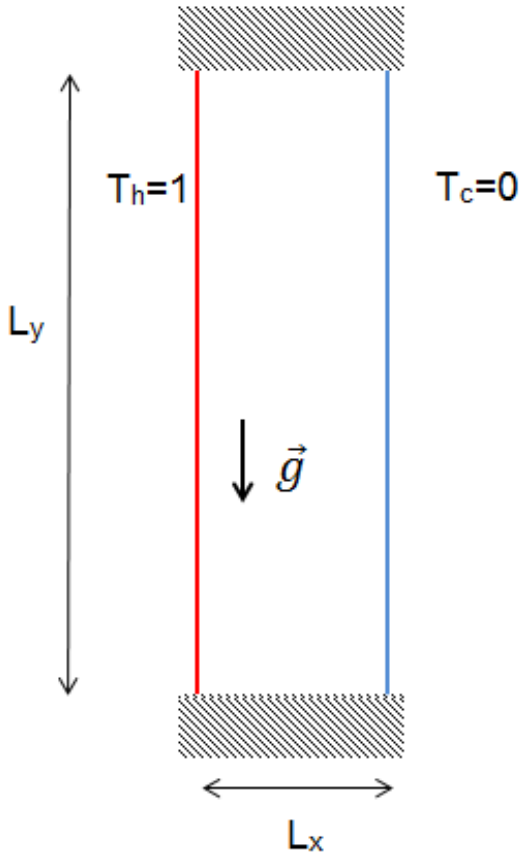

Figure 8.7 Schematic for the turbulence problem

As in the previous natural convection excersise, the solution algorithm will be the following:

- Evaluation of $R(u^n)$
- Evaluate u^p
- Evaluate $\boldsymbol{\nabla} \cdot \boldsymbol{u^p}$ and solve the discrete Poisson equation
- Obtain the new velocity field
- Evaluation of $R(T^n)$
- Obtain the new Temperature field

The mesh geometry in this case will be arranged in a different way. Since there are temeprature gradientes near the wall it is convenient to concentrate the mesh in this area. In order to do so, the control volumes are distributed using the following function:

(Eq. 8.43)

$$(x_i)_j = \frac{L_i}{2}\left(1 + \frac{\tanh\left[\gamma_i \frac{2(j-1)}{N_i} - 1\right]}{\tanh \gamma_i}\right)$$

It is convenient to mention that since the symmetry of the diffusive term only depends on the geometry it will be checked only once at the beginning of the simmulation. On the other hand the convective term symmetry will be checked continuously in order to make sure that the properties of the equations are being conserved. According to the literature, a flow enclosed in a cavity with a 4:1 ratio, starts being caotic at a Rayleigh number of: 2.3×10^8 (35). For this section, two turbulent cases will be analysed: 6.4×10^8 and 2.0×10^9. As previously mentioned, as the simulation is running is necessary to have certain tracking points to check the progress and determine if a stadistically steady state has been reached.The figures below show an example of the time averaging plots for the horizontal and vertical velocities.

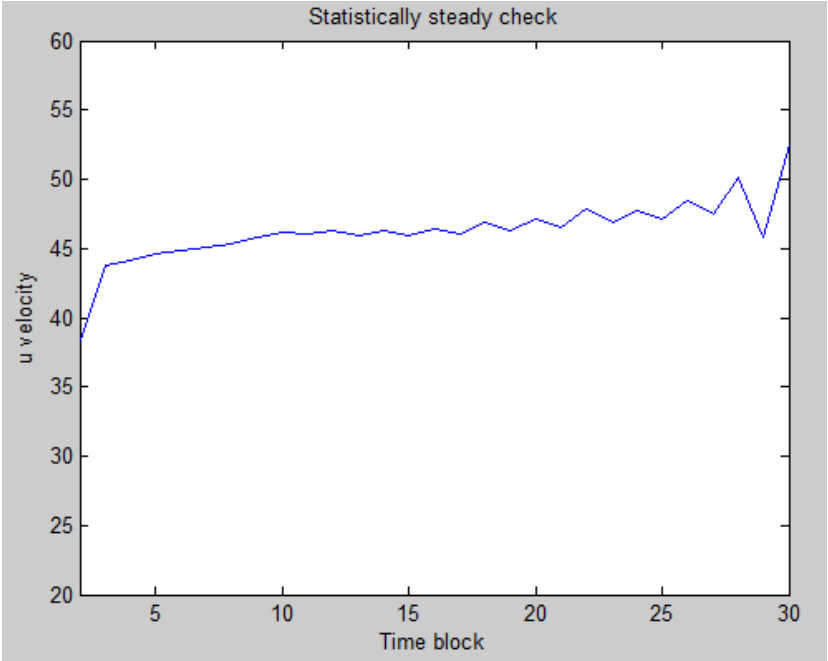

Figure 8.9. Horizontal velocity statistically steady check

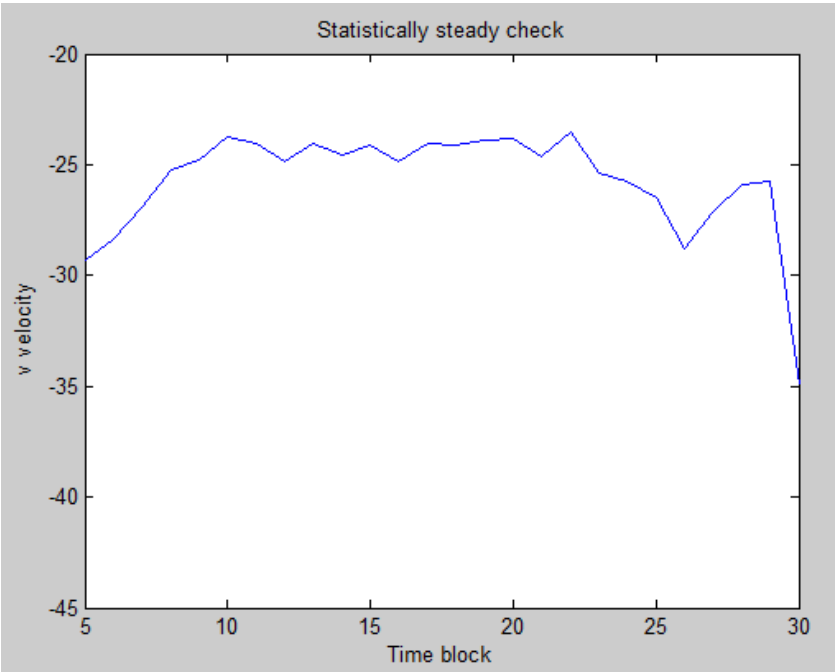

Figure 8.8. Vertical velocity statistically steady check

From the figures above, it can be stated that around time block 15, there is a zone where changes in the curve are minimal. This time block will be chosen as the point in time where properties (velocities and temperature will be evaluated). Once the whole domain has been post processed, the results for streamlines and temperature contours are shown in the next figure:

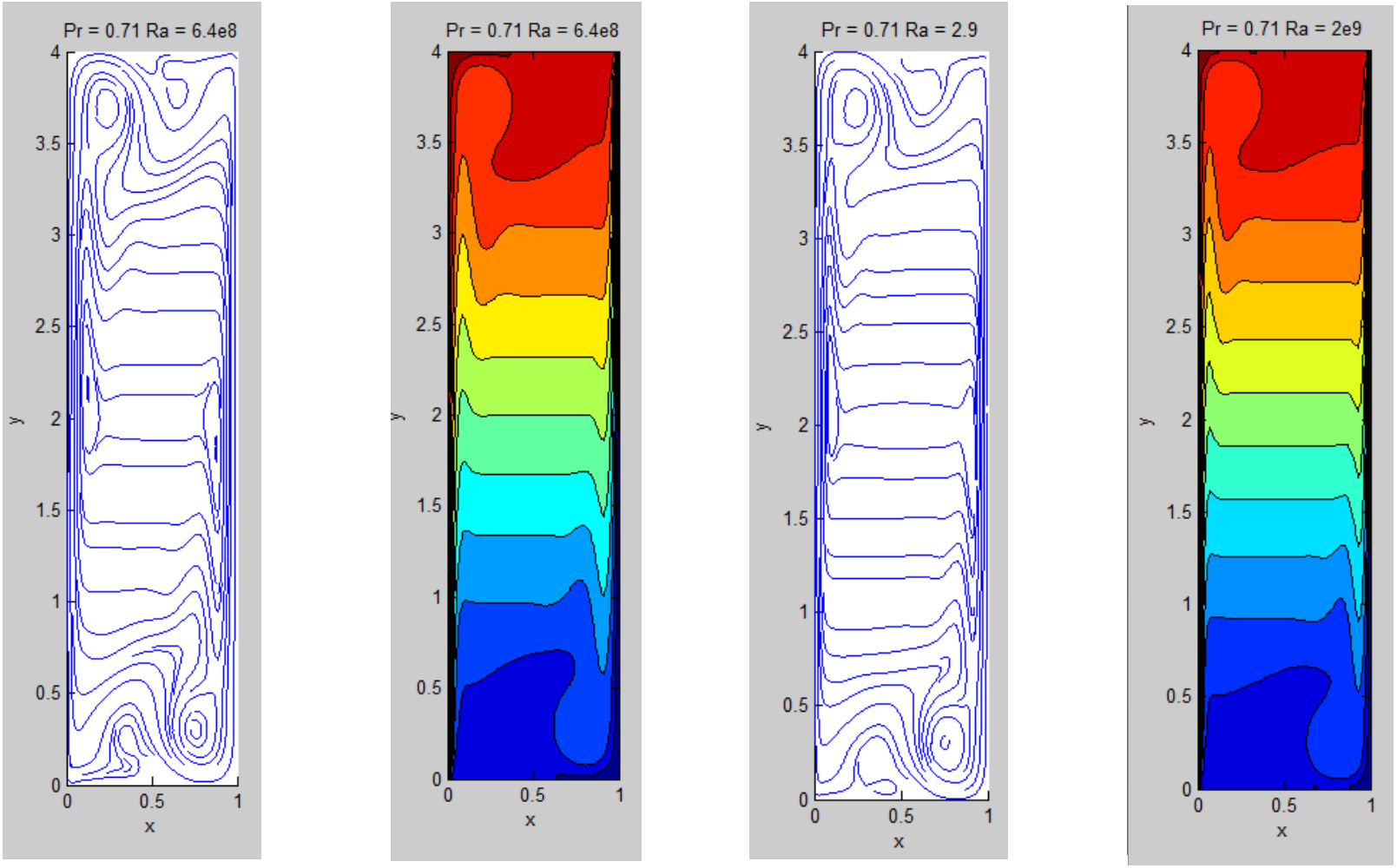

Figure 8.9. Streamlines and temperature contours. a) Ra=6.4e8 b) Ra=2e9

The results of the simulation are in good agreement with the benchmark solution, the reader is invited to check the comparison table in section 4 in the Appendix. The following figures show the plot of the temperature as a function of height at mid-width. As can be seen in the previous plots, the corners of the cavity concentrate the largest eddies, while the center of the cavity seems to show a stratified profile for both velocity and temperature.

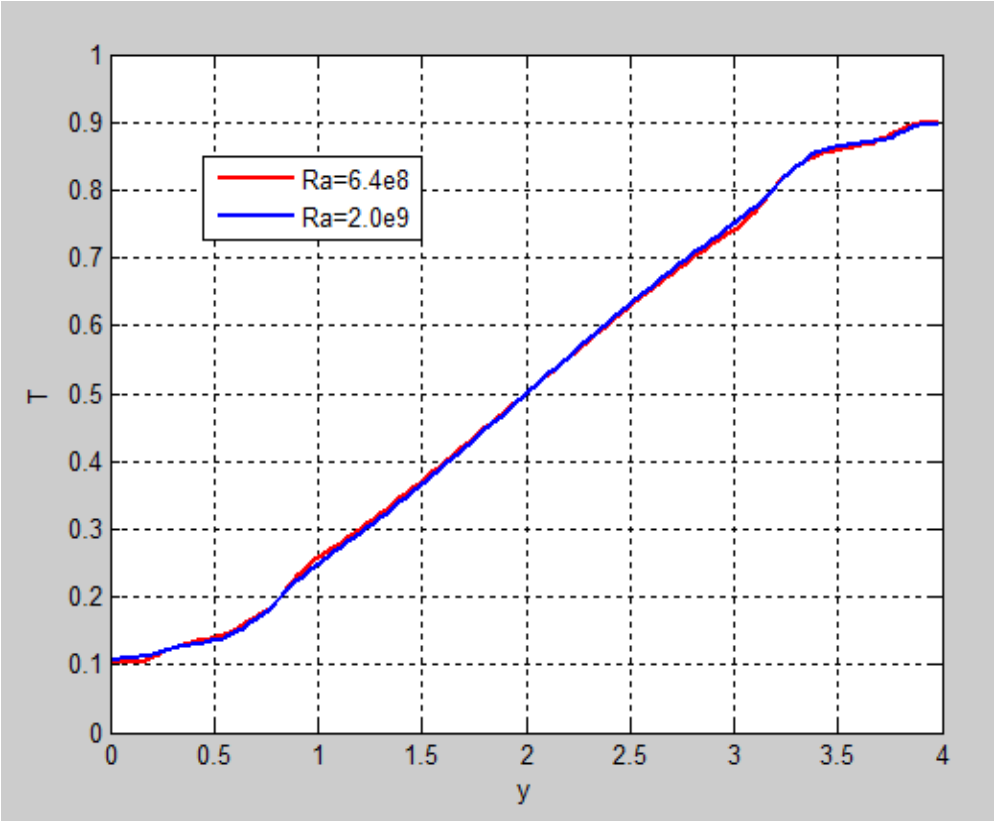

Figure 8.10. Temperature plot at cavity mid-width

Analysis of the results

The energy spectrum plot for the direct numerical simulation (DNS) is a smooth curve with a negative slope. In the energy containing range the behavior is almost linear. For the small scales the slope is steeper. When the simulation was performed considering only 20 modes, the curve was unstable and not representing accurately the DNS energy spectrum. A Large Eddy simulation (LES) model was proposed. With this model the kinematic viscosity was modified introducing a spectral eddy-viscosity model. The curve of the energy spectrum featuring LES was more accurate in the energy containing range. The rest of the ranges

were filtered and does not appear in the curve. Regarding symmetry preserving it can be commented that when evaluating the convective term, the analysis can be performed with a mass balance in the faces of the control volume of a control volume. The diffusive operator is evaluated through a geometry analysis and finally the gradient and divergence operators are related via the Poisson equation.

Regarding the exercise of the turbulent direct numerical simulation, the conclusions were the following. The time integration for the first case considered a total simulation time of 0.3 seconds while the integration time was 0.15 seconds. For the second case, it took 10 seconds to achieve a statistically static state and the integration period was determined to be 8 seconds. The streamlines show a stratified behavior in the center part of the cavity. Eddies start to form at the upper-left and bottom-right corners. The streamlines for both Rayleigh numbers feature symmetry in the horizontal and vertical axis. The temperature profile closely resembles the streamlines pattern showing a stratified area in the center of the cavity. Figure 8.10 shows that the temperature profile at the mid-with of the simulation is very similar for $Ra=6.4x10^8$ and $Ra=2.0x10^9$. The curve features a linear behavior at the center of the cavity.

Conclusions

Heat transfer in flows in motion is a complex issue that is broadly found in engineering applications. In most cases, physical experiments are resource consuming or practically unfeasible. Numerical simulations have proven to be a useful tool to model the flow behavior in a simple and fast way. In this work, some insights on numerical methods and computational fluid dynamics were addressed. From the first section, it can be concluded that renewables are a necessary alternative to cope with the increasing energy demand. Unlike fossil fuels, renewables provide a clean and secure supply of power. Among renewables, solar energy is gaining momentum with new projects all over the world. Specifically, Concentrated Solar Power technologies are turning into an interesting market to invest and develop. Even though the technology is on its early stages, CFD analysis can contribute to explain the working of the installation and predict the system thermal losses.

From the heat conduction section it was shown how thermal energy is transferred within a domain. First, it was shown how the heat transfer is described via the Fourier's law. In this equation, the thermal conductivity plays an important role. It was shown how this term can be approximated when there is an interface between two different materials using a concept called harmonic mean. Furthermore, the discretization and numerical resolution of Laplace operators found in conduction only problems was introduced. The boundary conditions treatment was also introduced and was extensively used throughout the thesis work. Finally, it was found that once the discretized equations are formed, their resolution can be performed with algorithms such as Gauss-Seidel or TDMA.

From the convection-diffusion section, it was seen that there are many schemes to approximate the convective term in the energy equations. According to the flow characteristics some schemes are more efficient than others. The power-law scheme was proven to be the best regarding accuracy but the computational costs are also high when working with fine meshes. Additionally it was found that when the mesh is fine enough, the numerical results are very similar to the ones from the analytic solution.

The Navier-Stokes equations section was very useful to understand the driving mechanism of flow motion. An early fundamental concept was the staggered grid arrangement. In this form, the velocity and pressure variables are decoupled and stored in the faces and the center of the control volumes respectively. It was found that the Fractional Step Method is a reliable and efficient way to solve the momentum equation with a low computational cost. The continuity constraint is introduced via a Poisson equation, which assures that the mass balance in the system is complied.

The differentially heated square cavity was one of the most challenging exercises solved in this thesis. Its complexity comes from the fact that the energy and momentum equations need to be solved simultaneously. As the previous exercise, a central difference scheme was used and the results were accurate. The Nusselt number is a direct indicator of the heat losses due to convection. It was found that this number was directly proportional to the Rayleigh number of the simulation.

Computational fluid dynamics is not constrained by the uniform nature of a mesh. It was found that through a different integration and discretization procedure it is possible to work on unstructured meshes that can fit in a better way the geometry of a problem. The drawback of this type of meshes is that the information dealing with the connectivity between nodes requires more storage capabilities than a conventional structured mesh.

Turbulence is a complex and still developing theory. Numerical approximations are available to help understand the chaotic nature of this phenomenon. It was seen how the scales of motion of turbulent flow can be represented in a Fourier space. With this information, it is possible to get the energy spectrum and test how the kinetic energy is transferred from the large scales to the slow scales and finally dissipated through viscosity. It was also found that in order for the discretized equations to solve the system mimicking the properties of a continuum, symmetry preservation has to be achieved. The convective symmetry preservation is checked via a mass balance on each control volume. The diffusive term is evaluated via a geometry analysis. Finally a time averaging integration process was used to determine the mean properties of a turbulent flow: temperature and velocities.

The future work will include further analysis on turbulent flows. Concepts like second-order statistics, the distribution of kinetic energy and probability density functions will be extensively examined. In the energy cascade section the Large Eddy Simulation model was briefly addressed. Future work will also include analysis of practical cases using this model.

Acknowledgements

I want to acknowledge the kind support of the professors and colleagues from CTTC Terrassa, UPC. Especially I would like to thank Prof. Assensi Oliva, Prof. Carlos David Pérez Segarra and Prof. Xavi Trías for their help and collaboration with this thesis project.

This Master degree project would not have been possible without the support of the SELECT InnoEnnergy program. I am very grateful and honored to have been part in such amazing experience

I would like to thank all my family, friends, teachers and everyone who has supported and encouraged me.

Con cariño para mis papas, Delia y Victor. Y a mis hermanos, Oscar y Alex.

A mi abue Lupita.

.

References

1. *Energy and Human Evolution.* **Price, David.** Ithaca, NY : Springer, 1995, xxx.

2. *Coal and the Industrial Revolution, 1700-1869.* **Clark, Gregory y Jacks, David.** Davis, California : Global Price and Income History Group, 2004.

3. *World Energy Outlook 2012.* **International Energy Agency.** Paris, France : OECD, 2012.

4. *Chemical reaction model for oil and gas generation for type I and type II kerogen.* **Braun, Robert L. y Burnham, Alan K.** Livermore, CA : Lawrence Livermore National Laboratory, 1993.

5. *An introduction to the petroleum industry.* **Fagan, Alphonsus.** Newfoundland : Department of mines and energy. Government of Newfoundland and Labrador, 2003.

6. *Historical Oil Shocks.* **Hamilton, James D.** San Diego, CA : Department of Economics, University of San Diego, 2010.

7. *Estimating CO2 emissions from the combustion of petroleum derivatives. .* **Febrero, Eladio, et al.** Seville, Spain : s.n., 2008.

8. *Terrestrial carbon cycle dynamics under recent and future climate change.* **Matthews, Damon, Weaver , Andew y Meissner, Katrin J.** Victoria, British Columbia, Canada : School of Earth and Ocean Studies, University of Victoria, 2005.

9. *Sustainable Energy withouth the hot air.* **Mackay, David JC.** Cambridge, UK : Department of Physics, University of Cambridge, 2008.

10. *Greenhouse gasees factsheets.* **University of Michigan.** Ann Arbor, MI : Center for sustainable systems, 2002.

11. *Greenhouse gases and global warming.* **Wallington, Timothy J., et al.** Oxford UK : Encyclopedia of Life Support Systems, 2004.

12. *Emission scenarios in the face of fosil-fuel peaking.* **Brecha, Robert J.** Dayton, OH : Elsevier, 2007.

13. *Wind Energy Explained.* **Manwell, J.F. y McGowan, J.G.** Sussex, UK : Wiley, 2009.

14. *Radiation (Solar).* **Fu, Quiang.** Seattle, Washington, USA : Elsevier, 2003.

15. *SolarGis.* **GeoModel Solar.** Bratislava, Slovakia : s.n., 2013.

16. *Concentrated solar power: energy from mirrors.* **National Renewable Energy Laboratories.** Merriefield, Virginia, USA : Department of Energy, US, 2011.

17. *Assesment of Parabolic trough and power solar technology cost and performance forecasts.* **National Renewable Energy Laboratory.** Chicago, Illinois, USA : s.n., 2003.

18. *Concentrating solar power, a review of the technology.* **Muller-Steinhagen, Hans y Trieb, Franz.** Stuttgart, Germany : DLR, 2004.

19. *Power Tower Process Diagram.* **Flowserve.**

20. *Solar Energy Systems Design.* **Stine, W.B. y Harrigan, R.W.** Washington, D.C. : Wiley and Sons, 1986.

21. *Conservation law.* **Encyclopaedia Britannica.** s.l. : retrieved from http://global.britannica.com/EBchecked/topic/133427/conservation-law, 2013.

22. *Transport Phenomena.* **Bird, R. Byron, Stewart, Warren, E. y Lightfoot, Edwin N. .** Madison, Wisconsin, USA : Wiley, 2005.

23. *Fundamentals of Heat and Mass Transfer.* **Incropera, Frank, DeWitt, David P y Bergman, Theodore.** Washington, D.C. : Wiley, 2007.

24. *Numerical heat transfer and fluid flow.* **Patankar, Suhas V.** New York, USA : Hemishpere Publishing Corporation, 1980.

25. *An introduction to Computational Fluid Dynamics.* **Versteeg, H.K. y Malalasekera, W.** Essex, GB : Wiley and Sons. Inc, 1995.

26. *Introduction to the Fractional Step Method.* **CTTC, Centre Tecnològic de Transferència de Calor.** Terrassa, Spain : Universitat Politecnica de Catalunya, 2013.

27. *¨Uber die partiellen Differenzengleichungen der mathematischen Physik.* **Courant, R., Friedrichs, K y Lewy, H.** Germany : s.n., 1928, Vol. Mathematische Annalen.

28. *Heat and mass transfer handbook.* **Raithby, G.D. y Hollands, K.G.T.** Waterloo, Canada : University of Waterloo, 2013.

29. *Natural convection of air in a square cavity a benchmark numerical solution.* **Davis, G. De Vahl.** Kensington, Australia : University of New South Wales, 1983.

30. *Analysis of different numerical schemes for the resolution of convection-diffusion equations using finite-volume methods on three-dimensional unstructured grids.* **Perez-Segarra, C.D, et al.** Barcelona, Spain : Taylor & Francis, 2006.

31. *Turbulent Flows.* **Pope, Stephen B.** Cambridge, UK : Cambridge University Press, 2000.

32. *Weather Prediction by Numerical Processes.* **Richardson, L.F.** Cambridge, UK : Cambridge University Press, 1922.

33. *The local structure of turbulence in incompressible viscous fluid for very large Reynolds umbers.* **Kolmogorov, A.N.** Moscow, Russia : Dokl. Acad Nauk, 1941.

34. *Eddy viscosity in two and three dimensions.* **Kraichnan, Robert H.** Dublin, New Hapshire : J. Atmos. Sci, 2005.

35. *Direct numerical simulations of two- and three-dimensiona turbulent natural convection flows in a differentially heated cavity of aspect ratio 4.* **Trias, F.X, et al.**

36. *Transition to unsteadiness routes to chaos and simulation of turbulent flows in cavities heated from the side: a review of the present status.* **Le Quéré, P.** Cedex, France : Hewitt GF, 1994.

37. *SolarGis.* **GeoModel Solar s.r.o.** Bratislava, Slovakia : s.n., 2013.

Appendix

Section 1

Ap. 1. Comparison table Pe=10

Position x	Γ/ρ=10 Benchmark	Numerical Solution
0.0	1.989	1.9854
0.1	1.402	1.4174
0.2	1.146	1.1597
0.3	0.946	0.95937
0.4	0.775	0.78746
0.5	0.621	0.63332
0.6	0.480	0.49203
0.7	0.349	0.36099
0.8	0.227	0.23849
0.9	0.111	0.10018
1.0	0.000	0.011

Ap. 2. Comparison table Pe=1000

Position x	Γ/ρ=1000 Benchmark	Numerical Solution
0.0	2.0000	2.0000
0.1	1.9990	2.0000
0.2	1.9997	1.9991
0.3	1.9850	1.9708
0.4	1.8410	1.7185
0.5	0.9510	1.0122
0.6	0.1540	0.31114
0.7	0.0010	0.04322
0.8	0.0000	0.0024808
0.9	0.0000	0.00000
1.0	0.0000	0.00000

Ap. 3. Comparison table, Pe= $1x10^6$

Position x	Γ/ρ=1000000 Benchmark	Numerical Solution
0.0	2.0000	2.0000
0.1	2.0000	2.0000
0.2	2.0000	1.9998
0.3	1.9990	1.9857
0.4	1.9640	1.7737
0.5	1.0000	1.026
0.6	0.036	0.27419
0.7	0.001	0.02882
0.8	0.000	0.0011228
0.9	0.000	0.0000
1.0	0.000	0.0000

Section 2

Ap. 4. Lid driven cavity problem comparison table u-min

Re	u min-Reference	Calculated	Error %
100	-0.2109	-0.2131	1.04314841
1000	-0.3829	-0.3807	0.57456255
5000	-0.43643	-0.4352	0.28183214

Ap. 5. Lid driven cavity problem comparison table v-min

Re	v min-Reference	Calculated	Error %
100	-0.24553	-0.2523	2.75730053
1000	-0.5151	-0.5181	0.58241118
5000	-0.55408	-0.5601	1.08648571

Ap. 6. Lid driven cavity problem comparison table v-max

Re	v max-Reference	Calculated	Error %
100	0.17527	0.178	1.55759685
1000	0.37095	0.369	0.52567732
5000	0.43648	0.434	0.56818182

Section 3

Ap. 7. Comparison table, Natural convection, Ra=1000

Pr=0.71 Ra=1e3			
	32 x 32 Mesh		
	Numerical Solution	Benchmark Solution	Error %
u_{max}	3.643	3.649	0.165
y	0.8281	0.813	
v_{max}	3.688	3.697	0.244
x	0.1719	0.178	
Nu_0	1.12	1.117	0.268
Nu_{max}	1.5142	1.505	0.608
y	0.1094	0.092	
Nu_{min}	0.6899	0.692	0.304
y	0.9844	1	

Ap. 8. Comparison table, Natural convection, Ra=1e4

Pr=0.71 Ra=1e4			
	32 x 32 Mesh		
	Numerical Solution	Benchmark Solution	Error %
u_{max}	16.27	16.178	0.565
y	0.8281	0.823	
v_{max}	19.48	19.617	0.703
x	0.1094	0.119	
Nu_0	2.2686	2.238	1.349
Nu_{max}	3.6084	3.528	2.228
y	0.1406	0.143	
Nu_{min}	0.5919	0.586	0.997
y	0.9844	1	

Ap. 2. Comparison table, Natural convection, Ra= 1e5

	Pr=0.71 Ra=1e5		
	64 x 64 Mesh		
	Numerical Solution	Benchmark Solution	Error %
u_{max}	35.32	34.73	1.670
y	0.8516	0.855	
v_{max}	68.38	68.59	0.307
x	0.07031	0.066	
Nu_0	4.5609	4.509	1.138
Nu_{max}	7.9164	7.717	2.519
y	0.07031	0.081	
Nu_{min}	0.738	0.729	1.220
y	0.9922	1	

Section 4

Ap. 3. Average results for turbulent differentially heated cavity, Ra = 6.4e8

Parameter	Location	Benchmark	Numerical solution	Error %
$\bar{u}_{2,max}$	Mid-height plane	0.00087	0.00098	12.43
$\bar{u}_{3,max}$		0.22300	0.22330	0.13
$\bar{u}_{2,max}$	Mid-width plane	0.02320	0.01790	29.61
$\bar{u}_{3,max}$		0.04490	0.03630	23.69
$\bar{T}_{max}$		0.89300	0.89910	0.68

Ap. 11. Average results for turbulent differentially heated cavity, Ra= 2e9

Parameter	Location	Benchmark	Numerical solution	Error %
$\overline{u}_{2,max}$	Mid-height plane	0.00060	0.00064	6.13
$\overline{u}_{3,max}$		0.22300	0.22550	1.12
$\overline{u}_{2,max}$	Mid-width plane	0.02010	0.01700	18.24
$\overline{u}_{3,max}$		0.03630	0.03020	20.20
$\overline{T}_{max}$		0.89000	0.89740	0.83